InGaAs/GaAsSb Type-II superlattices grown on InP substrates for extended short-wave infrared photodetectors

Hu Yidan

Department of Physics

Lancaster University

A dissertation submitted for the degree of

Master of Science by Research in Physics

September 2025

Abstract

This thesis aims to explore the application feasibility of type II InGaAs/GaAsSb superlattice (T2SL) based on InP substrate epitaxial growth in extended shortwave infrared (e-SWIR) light detectors with a cut-off wavelength of more than 2.5 μm. The device structure was analysed by high-resolution X-ray diffraction (XRD), and the results showed that the superlattice had good crystallization quality and layer periodicity. Photoluminescence (PL) experiments further revealed the bandgap properties of the absorbing layer, with emission wavelengths consistent with the designed cut-off wavelength. The prepared PIN light detector exhibited a wide spectral response in the range of 2.25 to 6 μm, with a peak response between 1–1.5 μm, and its cut-off wavelength was consistent with the PL results, demonstrating the effectiveness of the type II InGaAs/GaAsSb SL absorbing layer. Compared to commercial devices, the best performing device in the A1769 wafer exhibited higher photo response intensity, but the response curve has slight fluctuations, which may be due to insufficient material uniformity. These results indicate that InP-based type-II InGaAs/GaAsSb superlattices have application potential in high-sensitivity e-SWIR light detectors, but they still need to be further optimized in terms of material uniformity and device fabrication process.

Acknowledgement

I would like to thank my supervisors, Dr. Qiandong Zhuang, Dr. Andy Marshall and Prof. Qiang Ni without whose endless support, kindness, and more importantly, patience, I would not be where I am today.

I would like to thank Matthew Bentley for his valuable support in sample growth and for his patient guidance and training during XRD, PL, IV, and light response testing. His expertise and selfless help have played an important role in the smooth development of this work.

Yidan Hu

Declaration

I declare that the work presented in this dissertation is, to the best of my knowledge and belief, original and my own work. The material has not been submitted, either in whole or in part, for a degree at this, or any other university. This dissertation does not exceed the maximum permitted word length of 35,000 words excluding the bibliography and appendices. A rough estimate of the word count is: 16194

Yidan Hu

Publications and Presentations

Published paper

Cao, P., Wei, J., Bentley, M., Davison, N., Hu, Y., You, M., ... & Zheng, W. (2025). nBn mid-wavelength infrared photodetectors based on bulk InGaAsSb absorbers. *Optical Materials Express*, *15*(4), 717-723.

Contents

Chapter 1 Introduction

1.1 Overview

Over the decades, optoelectronics operating in the shortwave infrared (SWIR) band in the range of 0.78 μm to 3 μm, have attracted increasing attention due to their applications in a wide range of important fields, for instance, night imaging[1], optical fiber communication[2], gas detection[3], and biomedical diagnostics[4]-[5]. Particularly, the SWIR is a powerful optical tool in biomedical applications, because of its deep penetration into biological tissues and the strong correlation with metabolic biomarkers, such as the detection of water, protein, glucose, pO_2, pCO_2 and lactate, and monitoring them can provide a solid foundation[6].

As key components in SWIR detection systems, infrared photodetectors have undergone decades of development across numerous materials platforms and technological approaches. HgCdTe (MCT), as one of the most promising semiconductors, has enabled photodetectors with high performance in terms of detectivity and tunable responsive spectral bands (from SWIR to long-wavelength IR). However, this material suffers from several challenges such as expensive costs, high toxicity of precursors,[7] poor uniformity[8], which yield in complexity in material growth and device manufacturing process hence difficulty for larger area focal plane array manufacturing.[9]Another promising candidate is III-V compound InGaAs which is lattice-matched to InP substrates, which has been successfully developed for telecom uses. However, the cut-off wavelength is restricted at 1650 nm due to its bandgap energy. In order to achieve photodetection at longer wavelengths, efforts have been made to extend the cut-off wavelength by increasing the Indium concentration within the InGaAs layer, leading to wavelength-extended InGaAs detectors with a cut-off wavelength up to 2.6 μm.[10] However, the large lattice mismatch between InGaAs and the InP substrate remains a critical issue, leading to the formation of a high density of dislocations that act as recombination centers and thus deteriorate the detector characteristics. Recently, the detection of SWIR based on InGaAs/GaAsSb type II superlattices (T2SLs) on InP substrates has emerged as a promising alternative,[11] which has attracted the interest of many researchers.[12] Extensive research efforts have been devoted to extending the detection wavelength with improved performance. In terms of devices and applications, InGaAsSb is relatively mature on GaSb substrates,

enabling high-performance mid-infrared lasers and low-dark-current detectors covering the 1.9–3.5 μm wavelength range, which are widely used in gas sensing, infrared countermeasures, and imaging[13]. On the InP substrate, the operating bands (to 2–3 μm and beyond) are expanded through buffer layers and strain engineering, and detectors and waveguide devices compatible with InP photonic integrated circuits are demonstrated with the potential of mid-infrared PICs [14]. However, the main issues with GaSb platforms are cost and thermal management, while InP platforms face challenges such as a high dislocation density and limited wavelength expansion due to lattice mismatch. In this study, we aim to demonstrate the feasibility of utilizing type-II InGaAs/GaAsSb SL on InP for e-SWIR infrared photodetectors with cut-off wavelength over 2.5 μm.

1.2 Literature review on e-SWIR photodetectors

At present, the bulk materials commonly used for shortwave infrared detection are high-In content $In_xGa_{1-x}As$ compounds. When the component of In is 0.53, $In_{0.53}Ga_{0.47}As$ is lattice-matched to the InP substrate, and has high responsivity in the spectral range of 0.9 μm to 1.7 μm, which completely covers the near-infrared band[15]. However, when the indium (In) composition exceeds 0.53, the lattice constant of the $In_xGa_{1-x}As$ compound increases, leading to compressive strain between the $In_xGa_{1-x}As$ layer and the InP substrate due to lattice mismatch. If the In content is increased to 78%, the compressive strain between $In_xGa_{1-x}As$ and InP substrates will reach about 1.7%.[16] The dark current of the device increases rapidly with increasing defect and dislocation density. In recent years, researchers have made considerable efforts to reduce the dark current of high-In In-component $In_xGa_{1-x}As$-based detectors. Zhang Y-G, et al. from the Shanghai Institute of Microsystems, Chinese Academy of Sciences, designed an In component step-type gradient $In_xAl_{1-x}As$ buffer layer.[17] In 2015, Gu Yi et al. designed an $In_{0.83}Ga_{0.17}As$ shortwave infrared detector with an InAs/InGaAs superlattice as the electronic barrier, with a 50% cut-off wavelength of 2.61 μm. [18] In 2001, Hoogeveen, R. W., et al. discussed the development of an extended wavelength InGaAs detector array for the SCIAMACHY instrument for space-based spectroscopic analysis of the Earth's atmosphere. The detector covers a spectral range of 1.0 to 2.4 μm, enhancing the ability to monitor atmospheric composition. [19]In 2021, Xuefei Li et al. used molecular beam epitaxy to study the growth of

extended wavelength InGaAs on a stepped InAsP buffer with undulating composition. They found that this approach enhances the material properties of InGaAs, making it more suitable for applications that require extended wavelength detection capabilities.

In recent years, researchers have also made a lot of efforts to study the use of extended-Wavelength InGaAsSb in SWIR. In 2018, Hongyue Hao et al[20]. reported an extended wavelength InGaAsSb infrared unipolar barrier detector operating at room temperature. The modified detector exhibited a detectivity (D*) of 2.2×10^{10} cm·Hz$^{1/2}$·W^{-1} at 200 K, which increased to 7.4×10^{11} cm·Hz$^{1/2}$·W^{-1} under optimized conditions. In 2025, Mamic, Katarina et al. demonstrated that InGaAsSb enables bandgap tuning over the wavelength range of 1.7–3 μm through adjustment of the In/As composition, while maintaining high absorbance and high quantum efficiency. When the indium content is low, InGaAsSb exhibits excellent performance, such as low dark current and high detectivity (D*)[22]. A monopole barrier structure has been designed to further improve SWIR performance by reducing dark current and increasing detection rates. The dark current density was 2.29×10^{-5} A/cm^2 at 0V bias at 77K. At room temperature the dark current at 0V bias was 4×10^{-3} A/cm^2 and the R0A reaching 44 cm^2. In 2021, I. Shafir[21] et al. reported a GaSb-matched molecular beam-epitaxy grown InGaAsSb p-n photodetector lattice intended for extended SWIR detection. Under frontal illumination, the photodetector exhibits a high quantum efficiency of 73% at room temperature, with a dark current density of 2.9×10^{-6} A/cm² at 200 K and 4.6 mA/cm² at 300 K (−0.1 V bias). The detection rate (D*) value

In addition, there have been some studies on Extended wavelength InAlAsSb in the SWIR range. In 2021, J. F. Klem[23] et al. reported the fabrication and characterization of AlInAsSb and InPAsSb nBn infrared detectors with cut-off wavelengths ranging from 2.55 to 3.25 μm at 200 K. The detector exhibits an external quantum efficiency of 40-50% at 50 mV reverse bias with no anti-reflection coating. The study highlights the potential of these materials to expand SWIR detection. In 2024, Dong Xiawei[24] et al. demonstrated that integrating a fully dielectric amorphous germanium photonic capture grating significantly improved the performance of Al0.3InAsSb PIN photodetectors for extended SWIR applications, including enhanced quantum efficiency and reduced dark current.

Sai-Halasz[25] et al. first reported the InGaAs/GaAsSb material system, lattice-matched to InP in 1977, and has since been recognized as a promising material for SWIR detection. In 2005, Sidhu

et al.[26] demonstrated an InP-based photodiode using InGaAs/GaAsSb type-II quantum wells, exhibiting a peak detectivity of 3.8×10^9 cm·√Hz·W^{-1} and a peak room-temperature responsivity of 0.64 A/W at a wavelength of 2.26 μm. It can be seen that the related research about T2SLs has developed since its early development. In 2011, Baile Chen et al.[27] compared two InGaAs/GaAsSb type-II photodiodes, one with a strain-compensated absorption region and the other with a lattice-matched absorption region. The devices exhibited optical responses up to 3.4 and 2.8 μm, with dark current densities of 9.7 and 1.66 mA/cm², respectively, at 290 K under −0.5 V reverse bias.

In recent years, researchers have focused on achieving extended-wavelength SWIR detection while reducing dark current. Among them, researchers have made great efforts in performance optimization and material engineering of detectors. Y. Uliel et al.[28]have studied a T2SL layer structure aimed for 2.4 μm cutoff detection. They used a Zn diffusion process to form a shallow p–n junction in the absorber and fabricated Mesa- and planar-type devices, which exhibited dark currents of 1.5 and 1.2 mA/cm², respectively, at 300 K under 50 mV. The best detectivity (D*) was achieved at −0.1 V, reaching 1.7×10^{10} cm·√Hz/W at 300 K and increasing to 1.7×10^{11} cm·√Hz/W at 220 K. In 2022, Armando Gil and other partners explored optical and electrical data by comparing the symmetric period thickness of 10 nm and 5.8 nm in p-i-n photodetectors, and they found that smaller period thickness yielded substantially increased quantum efficiency. They also found that T2SL absorber require a turn-on bias in order to achieve good EQE characteristics with a bandgap wavelength of 2.1 μm [29]. In 2024, Yan Liang et al. demonstrated an e-SWIR p-B-n photodetector which base on the InGaAs/GaAsSb type-II superlattice with $Al_{0.85}Ga_{0.15}AsSb$ barrier. These devices exhibit 50% and 100% cut-off wavelengths of 2.1 μm and 2.6 μm respectively at 300 K. The device exhibits a specific detectivity of 4.12×10^{10} cm·√Hz/W at 2.1 μm under -100 mV. For the complete lattice matching with InP substrates and compatibility with InP processes, it's a good way to further improve optimization of the epitaxial quality to make it suitable for SWIR FPA[30].

In addition to the application of InGaAs/GaAsSb with InP as substrate in SWIR, there are also InGaAs/GaAsSb T2SL with GaSb as substrate. J. F. Klem[31] et al. investigated a GaAsSb/InGaAs type II bilayer quantum well structure grown by molecular beam epitaxy for use in long-wavelength lasers on GaAs substrates. These structures exhibit room-temperature

photoluminescence at wavelengths up to 1.43 μm. Lasers with these active regions exhibit threshold current densities as low as 120 A/cm² at 1.17 μm.

In recent years, avalanche photodiodes (APDs) have been continuously optimized in terms of materials, structure, and integration technology. Traditionally, APD material systems include Si-APDs, InGaAs/InP APDs, and HgCdTe APDs, with Si-APDs mainly used for visible light and shortwave infrared (SWIR) detection. In 2012, Kirill A. Lozovoy[32] et al. reviewed the latest advances in silicon-based avalanche photodiodes and discussed their potential applications in biomedical imaging and other fields. InGaAs/InP APDs are commonly used for optical communication (1.3–1.55 μm), with InGaAs serving as the absorption layer and InP as the multiplication layer, providing low dark current and a high gain–bandwidth product. In 2006, N. Namekata[33] et al. investigated the performance of an InGaAs/InP APD using sine wave gating to achieve 800 MHz single-photon detection at 1550 nm. HgCdTe APDs are suitable for medium-wave and long-wave infrared (MWIR and LWIR) detection. In 2021, Jin Chen[34] et al. investigated a high-performance HgCdTe APD with a unipolar barrier structure, demonstrating its potential in applications such as 3D LiDAR. In recent years, many new APD material systems have emerged. For example, InGaAsSb/InAlAsSb APDs have been developed to operate at wavelengths above 2 μm. For example, InGaAsSb/InAlAsSb APD can be extended to wavelengths above 2 μm. In 2024, Hyemin Jung[35] et al. demonstrated an APD combining an InGaAs/GaAsSb type-II superlattice absorber and an AlGaAsSb multiplication layer, achieving high gain (M = 178) and low excess noise (F < 2, M < 20) at room temperature, suitable for detection at wavelengths greater than 2 μm, with an external quantum efficiency of 3560% at 2 μm. An external quantum efficiency of 3560% at 2 μm. Two-dimensional materials (such as MoS_2, graphene) have ultra-fast response speed and are suitable for next-generation optoelectronic devices. In 2023, Munir Ali[36] mentioned a graphene-silicon-based charge-coupled device pixel for non-destructively reading avalanche multiplication signals in silicon within the pixel. In 2023, Dekang Chen et al. proposed an APD design featuring photon-trapping (PT) microstructures plus an ultra-thin absorber (≈200 nm) in a Separate-Absorption, Charge, Multiplication (SACM) architecture using AlInAsSb alloy. By trapping incoming light within the thin layer, absorption is enhanced while dark current is suppressed.[37] In 2024, Hyemin Jung and other authors present a room-temperature linear-mode APD built on InP substrates. It utilizes A Type-II InGaAs/GaAsSb superlattice as the absorber, and an AlGaAsSb multiplication

layer—both lattice-matched to InP. This design leverages III–V manufacturability and the flexibility of superlattice engineering.[38]

InGaAs/GaAsSb superlattices (SL) have attracted significant interest due to their excellent band-engineering flexibility and precise tunability of bandgap, strain, and carrier confinement, making them promising for extended shortwave infrared (e-SWIR) and mid-infrared optoelectronic applications, including detectors and lasers. In this study, we characterized InGaAs, GaAsSb, InAlAsSb, and InGaAs/GaAsSb superlattices, analysed crystal mass, lattice matching, and strain by XRD, and studied their optical transitions and bandgap tunability by PL testing. These results provide important support for high-performance infrared detectors and laser structures based on antimony materials.

Chapter 2 Background Theory

This chapter mainly introduces the basic physics of semiconductors, p-n junctions, principle of photodetectors and IV Characteristics of p-n junctions.

2.1 Semiconductors

Semiconductors are a special class of materials with conductivity between conductor and insulator, and their conductivity can be adjusted by doping with different elements or changing external conditions such as temperature, pressure, and illumination. These are mainly due to the modification of the bandgap and the concentration of charge carriers in the materials[39]. To understand the physics of semiconductor materials, a simplified band gap diagram is commonly used. Figure 2.1.1 shows a typical band gap diagram. E_c denotes the conduction band energy (e.g., the bottom of parabolic conduction band) and E_v represents the valence band (e.g., the top of parabolic valence band). The energy difference between these is called the energy band gap (E_g) of the material. Below E_v, the valence band is fully occupied by electrons. Above conduction band E_c, there are few electrons which can freely move around and can be modified by doping. E_{vacuum} is the energy level of a free electron at rest just outside the surface. Electron affinity (χ) is the energy difference between the vacuum level and the conduction band minimum (CBM) of a semiconductor. For intrinsic semiconductors (not doped) the Fermi energy normally positioned around halfway between the valence band and the conduction band, regardless of the temperature.[40] however, its position can be shifted significantly by doping.

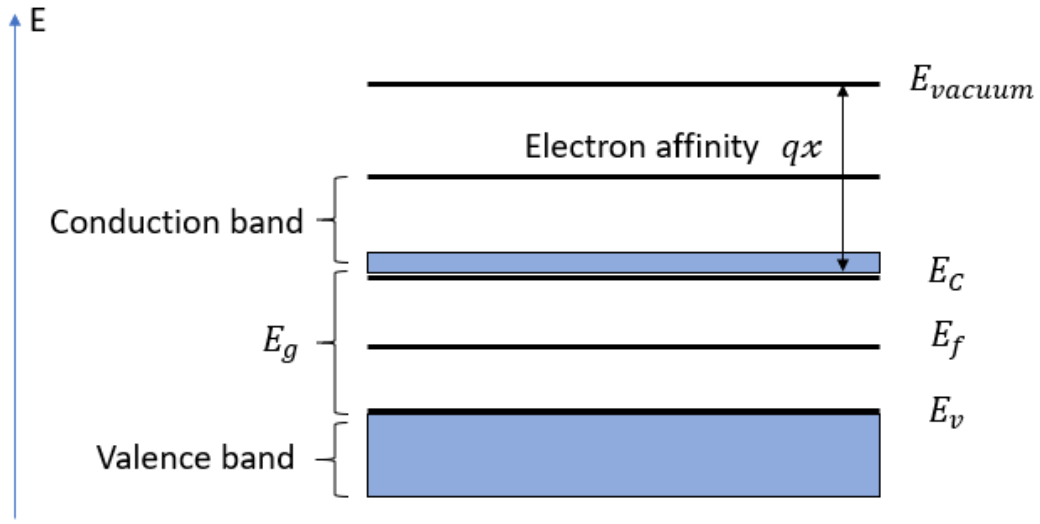

Figure 2.1.1 Simplified band gap diagram of semiconductors

The carrier concentration in semiconductors can be modified by doping. As shown in figure 2.1.2, doping will change the concentration of electrons and holes in semiconductor and then affect the position of Fermi level. n-type doping, such as the incorporation of pentavalent phosphorus (P) and arsenic (As) atoms into silicon, introduces extra free electrons into the conduction band, causing the Fermi level to move upward toward the conduction band edge; P-type doping, such as adding trivalent boron (B) and trivalent aluminium (Al), will introduce more holes into the valence band and make Fermi level move to the valence band. [41]

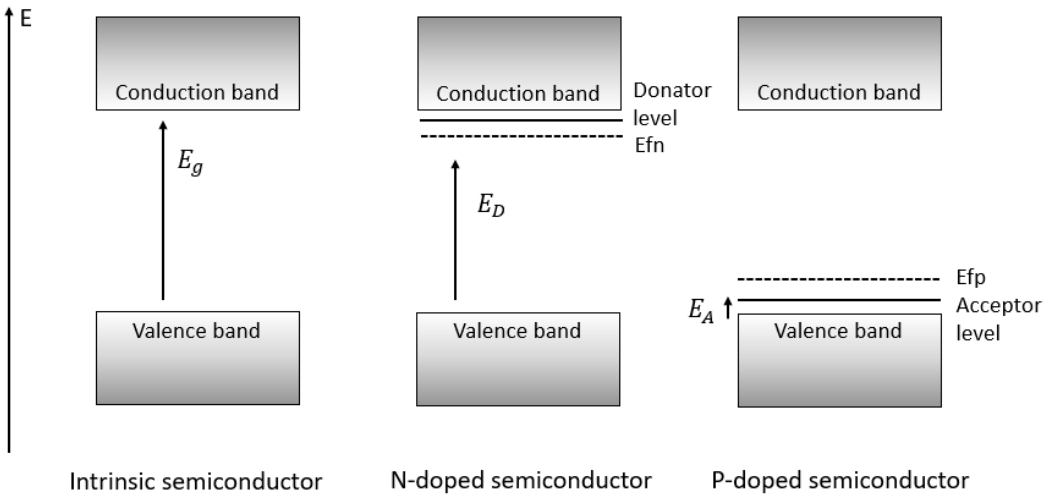

Figure 2.1.2 bandgap diagram of intrinsic semiconductor (a), N-doped semiconductor (b), P-doped semiconductor (c)

The bandgap energy E_g of a semiconductor is temperature-dependent quantity, which follows an empirical Varshni relationship[42]

$$E_g(T) = E_g(T=0) - \frac{\alpha T^2}{T+\beta} \tag{2.1.1}$$

where a and b are arshni parameters, T is temperature.

For ternary semiconductors, the bandgap energy can be expressed by the compositions of the binaries. [43]

$$E_g(A_{1-x}B_x) = (1-x)E_g(A) + xE_g(B) - x(1-x)C \tag{2.1.2}$$

Where C is bowing parameter which accounts for the deviation from a linear interpolation (virtual-crystal approximation) between the two binaries A and B, E_A and E_B are the bandgap energy of A and B respectively. An example is InGaAs:

$$E_g(GaAs_{1-x}InAs_x) = (1-x)E_g(GaAs) + xE_g(InAs) \tag{2.1.3}$$

Table (2.1.1) shows the major parameters of the major III-V semiconductor binaries.

Table 2.1.1 Parameters of the major III-V semiconductor binaries

Name	E_g (eV)	α (meV/K)	β (K)	E_g a(Å)
GaAs	1.519	0.5405	204	5.653
InAs	0.417	0.276	93	6.058
InP	1.4236	0.362	162	5.870
GaSb	0.812	0.417	140	6.096
InSb	0.235	0.32	170	6.479

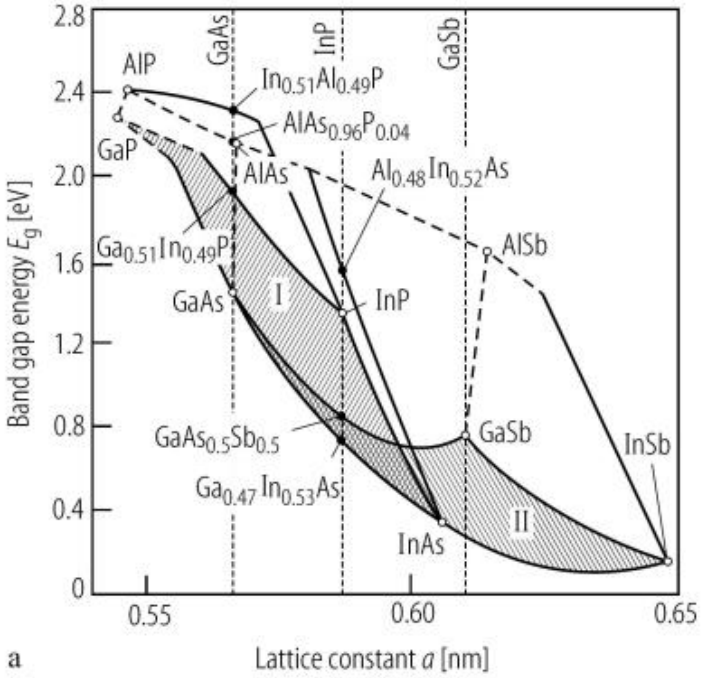

Figure 2.1.3 The band gap as a function of the lattice constant for various ternary III-V alloys.[44]

Another important physical property of semiconductors is their lattice constant. When a device structure contains more than two different semiconductors, their lattice constants must be identical or closely matched; otherwise, strain caused by lattice mismatch will develop and lead to the formation of dislocations. These dislocations will degrade the semiconductors properties and, hence, the corresponding device performance. Figure 2.1.3 shows the dependence of the band gap energy of major III–V compounds on lattice constant. This is widely used in semiconductor materials research to guide device design and heterostructure epitaxial growth[45]. The materials shown in the diagram include GaAs, InSb, AlSb, InP, etc. Each material is connected by its own line segments to form a series of possible combinations of ternary alloys (e.g., AlGaAs, InGaAs), which illustrate the variation of the band gap with alloy

composition. For example, lattice matched InGaAs on InP has a band gap energy of 0.74 eV at room temperature, corresponding to a wavelength in the near-infrared spectral range. Consequently, it is commonly used for telecommunication photodetectors. Another example is AlGaAs/GaAs heterostructures, which are widely used to construct quantum wells[46]. This is because AlGaAs alloys have wider bandgap energy than that of GaAs while maintaining a very close lattice constant to that of GaAs making them suitable for the fabrication of quantum structures. From this graph, we can also clearly see how these ternary compounds are lattice matched on the major substrates with corresponding alloy compositions.

2.2 p-n junction

A p–n junction is a fundamental structure in semiconductor devices. It is formed by combining p-type and n-type semiconductors. A p-type semiconductor contains acceptor impurities, and the dominant charge carriers are holes. An n-type semiconductor is doped with donor impurities, and the dominant charge carriers are electrons. The interface between these two semiconductors forms a special structure called a p–n junction.[47]

The formation of a p–n junction is achieved through doping processes. On a silicon wafer, a p-type region is formed on one side and an n-type region on the other side by different doping methods. As shown in Figure 2.2.1(a), at the junction between the p-type and n-type regions, electrons diffuse from the n region to the p region, while holes diffuse from the p region to the n region due to the concentration difference of charge carriers. This diffusion results in the formation of a space-charge region, also known as the depletion region[48]. Figure 2.2.1(b) shows that the depletion region contains an excess of fixed charges from ionized dopants and is free of mobile charge carriers. These ionized dopants create an internal electric field that prevents further diffusion of carriers across the junction. As a result, a space-charge region is established near the interface, giving rise to the p–n junction.

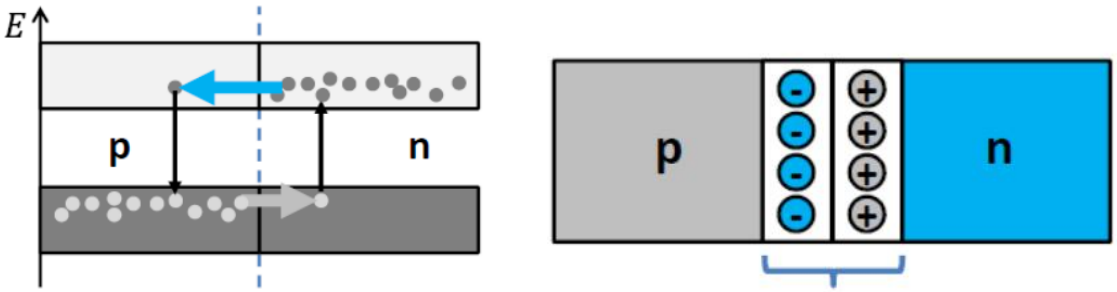

(a) (b)

Figure 2.2.1 Schematic diamgrams showing the formation of a PN junction, (a)The diffusing of electrons and holes , (b)The forming of a space charge region

Figure 2.2.2(a) shows the band gap energy diagram of a p–n junction under equilibrium conditions. Equilibrium means that the temperature inside the p–n junction is uniform and stable, and that the junction is not affected by external factors such as applied voltage or magnetic fields, resulting in macroscopic stability.[49] A space-charge region (depletion region) with a built-in electric field is formed at the p–n junction, extending from $-X_p$ to X_n. The direction of this electric field is from the n region to the p region, which drives holes toward the p region and electrons toward the n region, giving rise to drift currents that balance the diffusion currents.

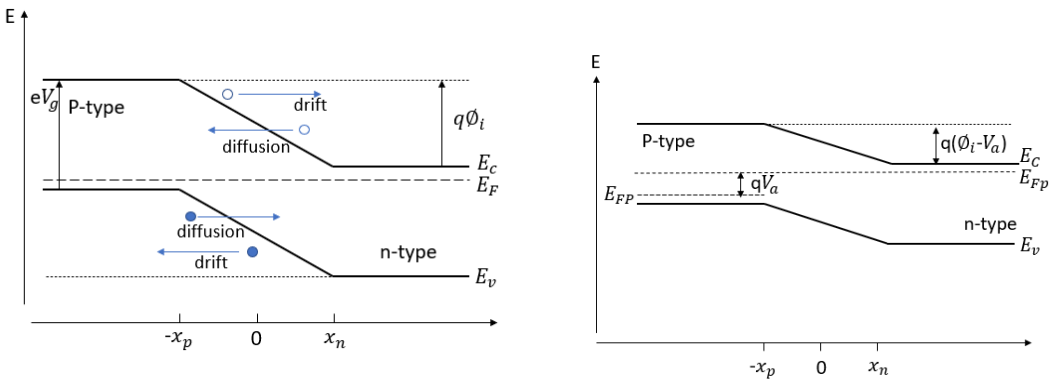

(a) (b)

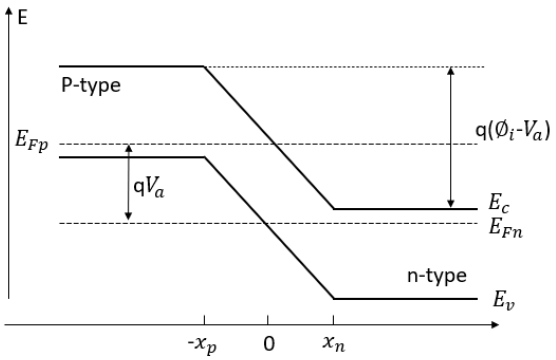

(c)

Figure 2.2.2 Bandgap energy diagram in equilibrium (a), forward bias (b) and reverse bias (c).

Figure 2.2.2 (b) shows the p-n junction under forward biased which means a positive voltage is applied to the p-type semiconductor side of the p-n junction while a negative voltage is applied to the n-type side, a potential barrier across the p-n junction is reduced, so the electrons and holes will be driven to the depletion region and causing current which increases with increased bias.[49]-[50] Meanwhile, the excess electrons and holes in the depletion region tend to combine and generate energies close to the band gap energy, thus, the p–n junction can act as a light emitter.[51]

Therefore, the luminescence intensity under forward bias reflects the competition between radiative and non-radiative recombination processes, and can be used as an important indicator of the material's optical quality. The radiative recombination results in the emission of photons, e.g., photoluminescence. The energy of the emitted photon is typically equal to or slightly less than the bandgap energy. Non-radiative recombination is associated with defects, impurities, or dislocations in the crystal. For these cases, the electron (or holes) first gets trapped by these defects and then recombines with a hole (or electron), releasing energy in the form of phonons, which heat the material, e.g. heat up the materials. In addition, There are three main types of Auger recombination. For this recombination, instead of generating a photon the energy released from the recombination of an electron-hole pair is transferred to a third carrier (another electron or hole) to be at a higher energy level, this third carrier then loses this excess energy to the lattice by emitting phonons (heat), not light. There are three

different Auger recombination as shown in figure 2.2.3. the competition between radiative and non-radiative recombination processes can be evaluated, providing insight into the optical quality of the material.

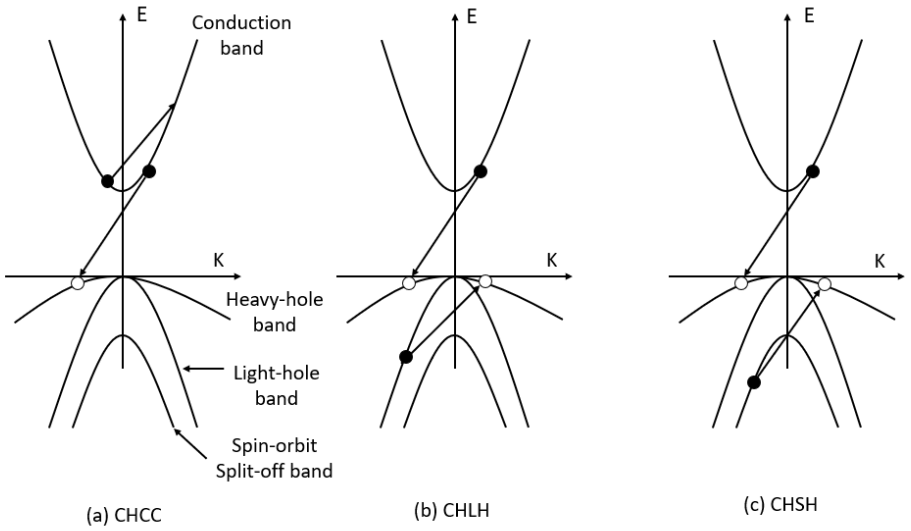

Figure 2.2.3 Three tapes of Auger recombination

When a p-n junction is under reverse bias, the depletion width increases and so does the built-in potential, greatly reducing the diffusion currents.[52] A negative voltage is applied to the p-type side of the p–n junction, while a positive voltage is applied to the n-type side, increasing the potential barrier across the junction. As a result, electrons and holes are unable to cross the p–n junction, and the resulting current is extremely small. Consequently, the resistance of the p–n junction becomes very large, and the junction exhibits nonlinear resistance characteristics. Under reverse bias, the widened depletion region generates a strong electric field. Electron–hole pairs generated by incident photons within the depletion region are separated by this electric field, forming a photocurrent. Therefore, a p–n junction can be used as a photodetector[53]. The detailed working principle of photodetector will be discussed in section 2.3.

2.3 Photodetectors

From figure 2.2.2, it can be seen that after the bias voltage V is applied, a minority carrier diffusion region appears. In the minority carrier diffusion region, the minority carrier Fermi level will rise or fall to be equal to the multi-carrier Fermi level, and the change of the distance between Fermi level and energy band corresponds to the change of carrier concentration.[54]-[56] The higher the carrier concentration, the closer the electron Fermi level is to the conduction band, and the closer the hole Fermi level is to the valence band. And the relative position of E_{Fn} and E_{Fp} will change under these two bias voltages. When p-n junction is in the positive bias, $E_{Fn} > E_{Fp}$; When p-n junction is in the reverse bias, $E_{Fn} < E_{Fp}$.[57]

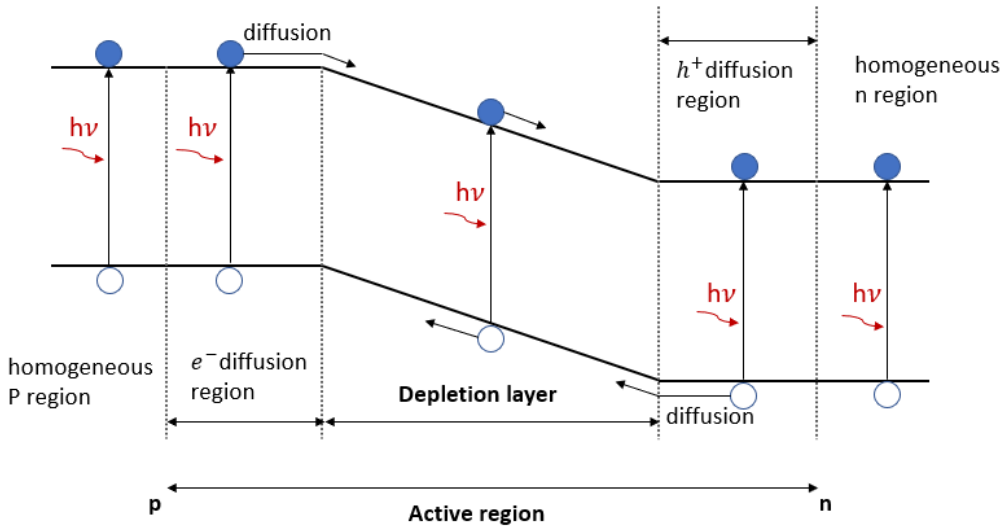

Figure 2.3.1 Photoexcitation of p-n junction photodiode

We can see from Figure 2.3.1 that when photons come from the left, there is a very good chance that the area close to the surface of the p–n junction absorbs the light and generates pairs of holes and electrons, but this region is very far from the depletion region. Therefore, these pairs do not contribute to the external current or voltage. We can clearly see the range of the active region that contributes to the external signal.

In the deeper absorption region, the generation of carriers close to the depletion region (electron diffusion region) allows these carriers to be easily separated by the built-in electric field, sweeping the electrons into the depletion region. This process contributes to the external signal. A similar mechanism occurs on the other side, called the hole diffusion region

.[58]-[59] where holes can be easily swept into the depletion region. In the depletion region, a large number of electron–hole pairs are generated by drift current under the action of the built-in electric field. At the same time, some electron–hole pairs on both sides of the depletion layer enter the depletion layer due to diffusion, forming the diffusion current.

2.4 IV characteristics

The Current-Voltage (IV) characteristic of a p-n junction is determined by the following relationship[60]:

$$I = I_0 \left[e^{\left(\frac{eV}{n_{id} k_B T}\right)} - 1 \right] \tag{2.4.1}$$

Where I_0 is the reverse saturation current, when V<<0, $I_s \approx -I_S$. V is the applied voltage, n is a material dependent constant (between 1 and 2), k is the Boltzmann constant, and T is temperature.

From Equation (2.4.1), we can see that the current increases exponentially under forward bias but remains at a low level under reverse bias (dark current). When the reverse voltage is sufficiently high, the device experiences a sharp increase in dark current, known as the breakdown voltage (V_{bd}). This behaviour is attributed to avalanche multiplication and quantum mechanical tunnelling. Since the dark current is very small under reverse bias while the current increases rapidly under forward bias, this behaviour is generally called a rectifying characteristic. Figure 6.3.1 shows the IV characteristic of a fabricated p–n junction, demonstrating a clear rectifying behaviour. An IV measurement of a p–n device is the primary examination used to evaluate the success of material growth and device fabrication.

Chapter 3 Experimental methods

3.1 X-ray Diffraction crystallography

The working principle of X-ray diffractometer crystallography (XRD) is based on the diffraction of X-rays by crystals. X-rays are electromagnetic waves with high energy, short wavelengths, and wavelengths comparable to the lattice constants of crystals. When X-rays shine on a crystal, they are scattered by many atoms within the crystal. Because of the regular atomic arrangement in the crystal, these scattered waves interfere with each other and produce diffraction phenomena. The intensity of the diffracted rays is strengthened in some directions and weakened in others, depending on whether constructive or destructive interference occurs. By analysing these diffraction results, structural information about the crystal, such as crystal plane spacing, unit cell type, and crystalline quality, can be obtained.

The detailed physics of XRD is complex, but we will only discuss the most important principle of XRD: Bragg diffraction. Bragg diffraction is a special case of Laue diffraction, which assumes that the reflection is specular and that the lattice atoms of the sample are distributed over a plane.[61] As shown in Figure 3.1.1, the wavelength of X-rays is comparable to the distance between atomic planes inside the crystal, so the crystal acts as a special grating for X-rays. When a beam of X-rays shines on the crystal, each atom produces scattered waves that interfere with each other to form a diffraction pattern. This interference is described by Bragg's equation:

$$(2d\sin\theta=n\lambda) \tag{3.1.1}$$

where θ is the incident angle, d is the crystal plane spacing, n is the diffraction order, and λ is the wavelength of incident ray.

For constructive interference to occur, the path length difference between beams reflected from adjacent atomic planes must be an integer multiple (n) of the wavelength (λ). This condition determines whether X-rays can interfere coherently within the crystal and thus produce diffraction. By measuring the Bragg diffraction angle, the lattice constant can be determined, which in turn allows the composition of an alloy to be inferred.

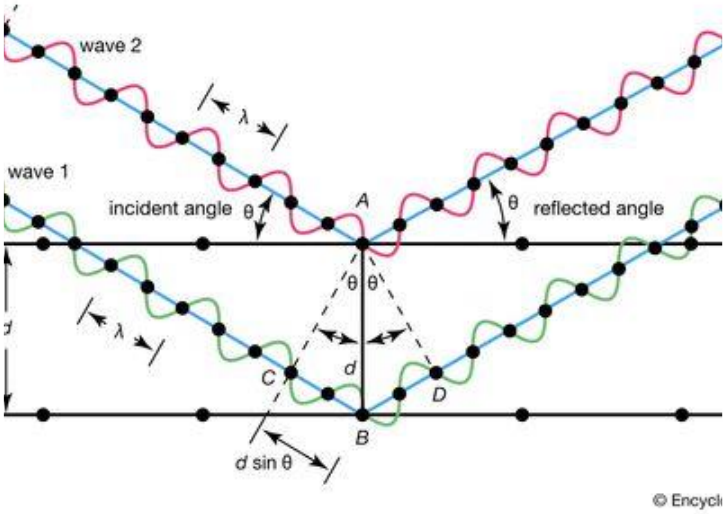

Figure 3.1.1 Schematic diagram showing the principle of X-ray diffraction in a crystal[62]

3.2 Photoluminescence (PL)

PL is a fundamental technique to investigate the optical properties of semiconductors[63].

The basic method for measuring the photoluminescence of semiconductor materials is to illuminate the sample surface with laser light of an appropriate photon energy (laser wavelength) and to measure the emitted photoluminescence. When the photon energy of the laser is larger than the bandgap energy (E_g) of the semiconductor, the laser light is absorbed and excites electrons from the valence band to the conduction band, creating electron–hole pairs. These photo-generated carriers tend to relax to lower-energy states and release the excess energy through either radiative or non-radiative recombination. Radiative recombination results in the emission of photons, i.e., photoluminescence, and the energy of the emitted photons is typically equal to or slightly less than the bandgap energy. Non-radiative recombination is commonly associated with defects, impurities, or dislocations in the crystal.

The intensity of photoluminescence is normally weak, particularly for semiconductors with smaller bandgap energies, where Auger recombination is stronger. Therefore, luminescence detection is usually performed using a lock-in amplifier[64]. In addition, by looking at luminescence at reduced temperatures, up to liquid helium temperature (4.2K), combined

with varied laser power, we can have a better understanding on the semiconductor structures being studied.

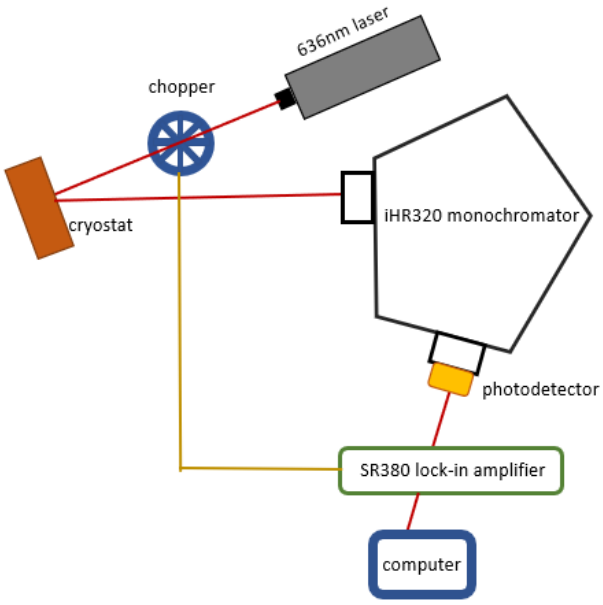

Figure 3.2.2 Schematic diagram of the photoluminescence system

Figure 3.2.2 illustrates the photoluminescence system was used for this project. The laser light source is provided by a 635 nm laser (OBIS S181006009, Coherent Ltd, US) which was controlled by the OBIS Coherent Connection software. This software could change the laser power[65]. A cryostat (Microstate-He, Oxford Instruments, UK) was used to control the sample temperature, it can load three experimental samples including one reference sample InAs. Because copper is a good conductive material, so the Samples were mounted onto a copper mount and the mount screwed to the end of the removeable cryostat arm—leveraging copper's high thermal conductivity advantages[66]. The cryostat was maintained in vacuum. We used a rough pump (Adixen Pfeiffer, Germany) firstly and then use a turbomolecular pump (HiCube 300Eco), to pump the cryostat till the pressure reached 10^{-4}mbar (measured by Edwards Vacuum, US)[67].

A helium transfer system is used to cool the sample to low temperatures. The helium transfer arm (LLT600 Siphon, Oxford Instruments, UK) is connected to a helium-4 dewar and inserted into the cryostat. Liquid helium is transferred into the cryostat to cool the sample, while helium

gas is removed through the transfer pipe attached to the needle-valve port.[68] After opening the liquid helium system, a temperature controller (Mercury iTC, Oxford Instruments, UK) is connected to the temperature sensor located in the cryostat heat exchanger. The Mercury iTC measures and controls the temperature with high precision and supports auxiliary cards for gas-flow management, such as automatic needle-valve operation[69]-[70]. The temperature is initially set to approximately 4.2 K and then gradually increased during measurements until noise interference becomes too large and no output signal can be detected. This continuous-flow helium cooling configuration is commonly used in low-temperature spectroscopy setups and provides a stable and precise thermal environment for optical measurements.

For measurements, the laser beam is directed onto the samples through a chopper wheel, operating at 50 Hz[71] to modulate the light and improve signal detection. The photoluminescence emitted from the sample is focused onto the entrance slit of an iHR320 monochromator using a pair of adjustable lenses. The iHR320 monochromator has a focal length of 320 mm and covers a spectral range from 150 to 1500 nm with a 1200 g/mm grating, and from 150 nm to 40 µm when equipped with appropriate gratings [73]. An InSb detector is used to detect the luminescence (cooled with liquid nitrogen), the output signal is passed to an internally constructed preamplifier and then to a lock-in amplifier (SR830, STAMFORD Instruments, USA). Using the chopper frequency as a reference signal for phase-sensitive detection[73]. The switching frequency is received as a reference signal, and the final signal is output to a computer.

SynerJY software (Horiba Jobin Yvon, France) is used for data acquisition, with the integration time held at 0.1 s for most measurements[75]. The spectra of an InAs reference sample are first collected to ensure that the system is properly optimized before measurements. Each sample is then scanned once at each laser power, with the excitation power ranging from 20 mW to 140 mW, and over a helium temperature range of 4.2–300 K[76]-[77]. For temperature-dependent measurements, the power remains constant at 140mW.

3.3 Spectral photo-response

A photoresponse setup is used to measure the spectral photoresponse of photodetectors grown by molecular beam epitaxy (MBE). The underlying mechanism is that when the photon energy is greater than or equal to the bandgap of the semiconductor material, the photon is absorbed and excites electrons from the valence band to the conduction band, forming electron–hole pairs. These carriers are then separated under the action of an external or built-in electric field, generating a photocurrent[78], Therefore, the operating principle of photodetectors is based on the photoelectric effect. The spectral response curve describes the relationship between the output signal and the incident optical power as a function of wavelength, and its shape is influenced by factors such as the material bandgap (which determines the cutoff wavelength), absorption coefficient, internal quantum efficiency, and carrier transport properties. [79] By measuring the spectral response, the energy band structure of the material can be analysed, the device quality can be evaluated, and essential data can be provided for photovoltaic material research and performance assessment.

Figure 3.3.1 illustrates the spectral photoresponse system used in this project. The light source is an SLS202 (Thorlabs, UK), a compact and highly stable broadband infrared tungsten halogen light source. The light passes through a chopper and then through a monochromator before illuminating the diode under test (DUT), following a configuration similar to that of the photoluminescence system described above. A resistor box is connected in series with the DUT, allowing the lock-in amplifier to measure the voltage drop across the resistor. A preamplifier is placed between the DUT and the lock-in amplifier to amplify the weak signal from the resistor box, enabling effective phase-sensitive detection by the subsequent lock-in amplifier (LIA). The chopper frequency is used as the reference signal, and the final processed signal is output to a computer.

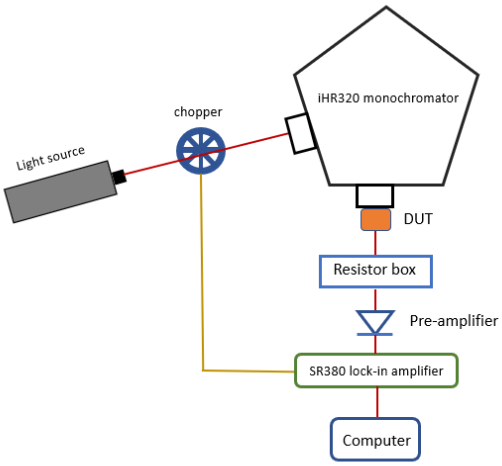

Figure 3.3.1 Schematic of the Spectral photo-response system

3.4 IV Measurement

Current–voltage (I–V) measurements are a fundamental method for evaluating the electrical properties of optoelectronic devices. By applying different bias voltages across the device terminals and measuring the corresponding current, the I–V characteristic curve can be obtained. This curve provides key information about device performance parameters, such as turn-on voltage, breakdown voltage, series resistance, and leakage current.

Figure 3.4.1 shows the set-up of IV probe station, a source-measurement unit (SMU) simultaneously applies a forward/reverse bias voltage across the two terminals of the DUT and measures the resultant current flowing through the DUT. The equipment is either an HP 4140B Pico ammeter, a Keithley 2400 SMU, and the software of data acquisition is LabVIEW.

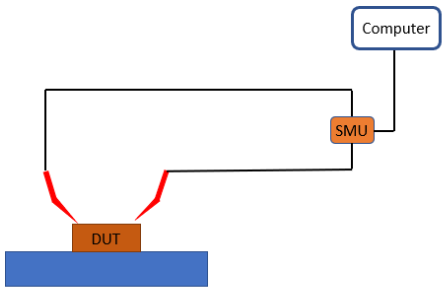

Figure 3.4.1 IV prob station

Chapter 4 Structural analysis

To realize type-II superlattice (T2SL) e-SWIR photodetectors on InP, molecular beam epitaxy (MBE) growth of four lattice-matched materials on InP was carried out, including InGaAs, GaAsSb, AlInAsSb, and InGaAs/GaAsSb T2SL. Multiple growth attempts were performed for each material. The resulting samples were characterized by X-ray diffraction (XRD) to determine their actual structures and compositions. Examples include 200-nm-thick InGaAs on InP, 200-nm-thick GaAsSb on InP, AlInAsSb on InP, and 40-period InGaAs/GaAsSb T2SL on InP.

4.1 InGaAs on InP

A set of InGaAs single epilayers were grown on InP at various indium and gallium cell temperatures to achieve lattice-matched InGaAs. Figure 4.1.1 shows X-ray diffraction (XRD) patterns of four InGaAs samples on InP. Two peaks are present for each sample: one located at 31.670° corresponds to the InP substrate, and the other originates from the InGaAs epilayer. All samples exhibit an epilayer peak close to the InP peak, indicating a small lattice mismatch and no relaxation, which was assumed in our simulations [80]. The detailed XRD parameters for these four samples are summarized in Table 4.1.1. Each sample shows a strong epilayer peak with a narrow full width at half maximum (FWHM) of 1.56–2.28 arcsec. In addition, Pendellösung fringes are observed, indicating high crystalline quality of the epilayers. The simulated structural parameters are listed in Tables 4.1 and 4.2, showing that sample A1636 has a nearly lattice-matched composition with a narrow FWHM of 1.56 arcsec.

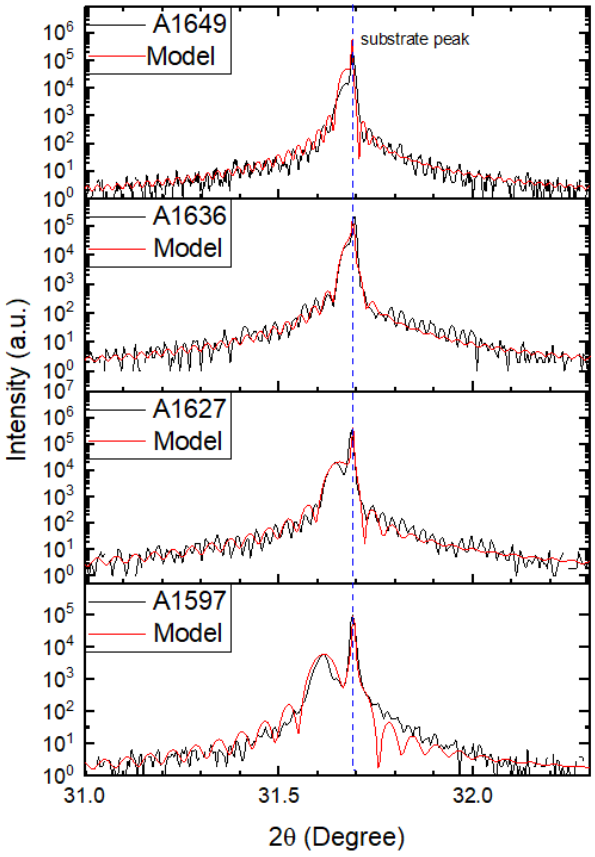

Figure 4.1.1 X-ray diffraction for the four samples of InGaAs on InP

Table 4.1.1 X-ray diffraction parameters for the samples of InGaAs/InP

Sample No	Structure	Epi angle (°)	Separation (°)	FWHM (')	In%	Thickness(nm)	Epi Intensity	Sub Intensity
A1597	InGaAs/InP	31.614	0.076	1.680	0.548	190.465	5933.960	97427.460
A1627	InGaAs/InP	31.626	0.039	2.280	0.540	164.424	20441.430	346195.520
A1636	InGaAs/InP	31.680	0.020	1.560	0.536	167.934	23523.750	223389.230
A1649	InGaAs/InP	31.661	0.019	1.680	0.537	151.953	14835.070	213335.050

Table 4.1.2 simulated composition, bandgap energy (0K) and relevant α, β for Vashini equaition

Name	Structure	InAs%	GaAs%	C(eV)	$\mathrm{E_g(eV), T = 0}$	a(Å)	α(meV/K)	$\beta(K)$
A1597	InGaAs/InP	0.548	0.452	0.150	0.878	5.386	0.473	143.172
A1627	InGaAs/InP	0.540	0.460	0.150	0.887	5.375	0.474	144.060
A1636	InGaAs/InP	0.536	0.464	0.150	0.891	5.369	0.474	144.504
A1649	InGaAs/InP	0.537	0.463	0.150	0.889	5.370	0.474	144.393

4.2 GaAsSb on InP

A set of GaAsSb single epilayers were grown on InP at various cell temperatures to achieve lattice-matched GaAsSb. Figure 4.2.1 shows X-ray diffraction (XRD) patterns of four GaAsSb samples on InP. Two peaks are present for each sample: one located at (angle) corresponds to the InP substrate, and the other originates from the GaAsSb epilayer. All samples exhibit an epilayer peak close to the InP peak, indicating a small lattice mismatch and no relaxation, which was assumed in our simulations. The detailed XRD parameters for these four samples are summarized in Table 4.2.1. Each sample shows a strong epilayer peak with a narrow full width at half maximum (FWHM) of 3.24–5.96 arcsec. In addition, Pendellösung fringes are observed, indicating high crystalline quality of the epilayers[81]-[82]. The simulated structural parameters are listed in Tables 4.2.1 and 4.2.2, showing that sample A1805 has a nearly lattice-matched composition with a narrow FWHM of 3.72 arcsec.

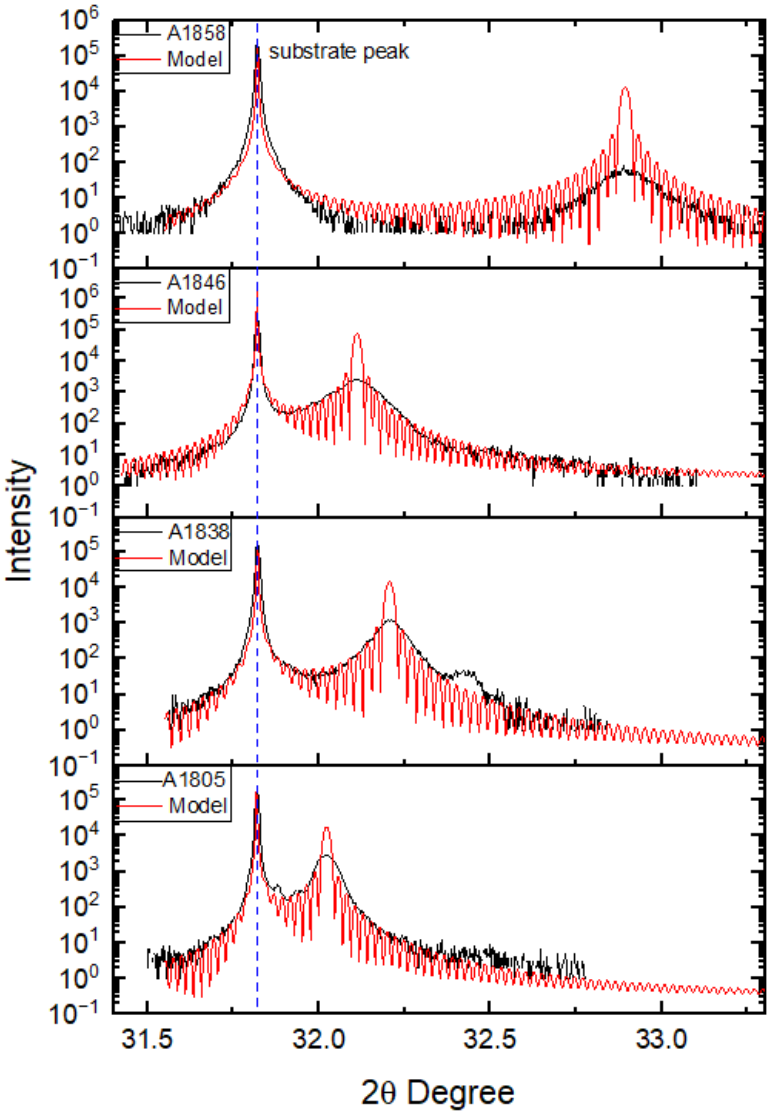

Figure 4.2.1 X-ray diffraction for the four samples of GaAsSb on InP

Table 4.2.1 X-ray diffraction parameters for the samples of GaAsSb/InP

Sample No	Structure	Epi angle (°)	Separation (°)	FWHM (')	As%	Thickness(nm)	Epi Intensity	Sub Intensity
A1838	GaAsSb/InP	32.043	0.381	3.240	0.588	200.000	1244.580	192726.556
A1846	GaAsSb/InP	32.089	0.293	5.964	0.570	230.000	2418.970	279043.321
A1858	GaAsSb/InP	32.888	1.071	4.920	0.720	200.000	74.218	207028.474
A1805	GaAsSb/InP	31.919	0.200	3.720	0.553	220.000	2828.869	166231.404

Table 4.2.2 simulated composition, bandgap energy (0K) and relevant α, β for Vashini equation

Name	Structure	GaAs%	GaSb%	C(eV)	$E_g(eV), T = 0$	a(Å)	α(meV/K)	$\beta(K)$
A1805	GaAsSb/InP	0.588	0.412	0.600	1.082	5.690	0.490	177.632
A1838	GaAsSb/InP	0.570	0.430	0.600	1.068	5.697	0.487	176.480
A1846	GaAsSb/InP	0.720	0.280	0.600	1.200	5.656	0.506	186.080
A1858	GaAsSb/InP	0.553	0.447	0.600	1.055	5.703	0.485	175.392

4.3 AlInAsSb on InP

A set of AlInAsSb single epilayers were grown on InP at various cell temperatures to achieve lattice-matched AlInAsSb. Figure 4.3.2 shows X-ray diffraction (XRD) patterns of six AlInAsSb samples on InP. Two peaks are present for each sample: one located at (angle) corresponds to the InP substrate, and the other originates from the AlInAsSb epilayer. All samples exhibit an epilayer peak close to the InP peak, indicating a small lattice mismatch and no relaxation, which was assumed in our simulations. The detailed XRD parameters for these six samples are summarized in Table 4.3.1. Each sample shows a strong epilayer peak with a narrow full width at half maximum (FWHM) of 2.160–13.200 arcsec. In addition, Pendellösung fringes are observed, indicating high crystalline quality of the epilayers[83]. Table 4.3.1. show that sample A1869 has a nearly matched composition with a narrow FMHW of 2.160 '.

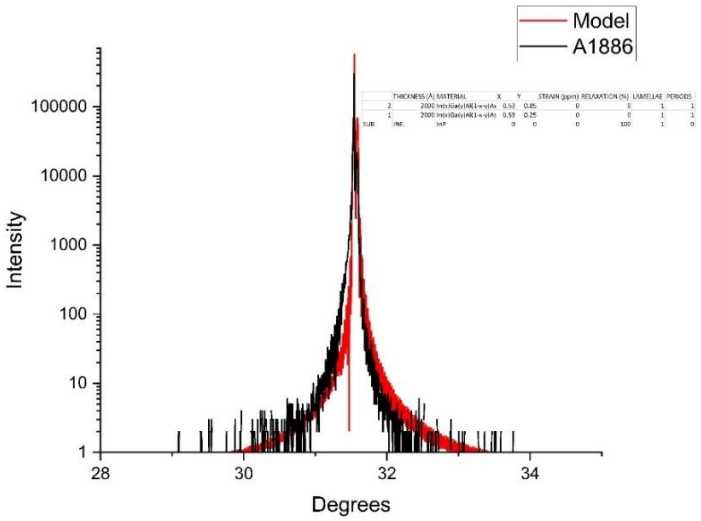

Figure 4.3.1 X-ray diffraction for the sample of AlInAsSb on InP(A1886)

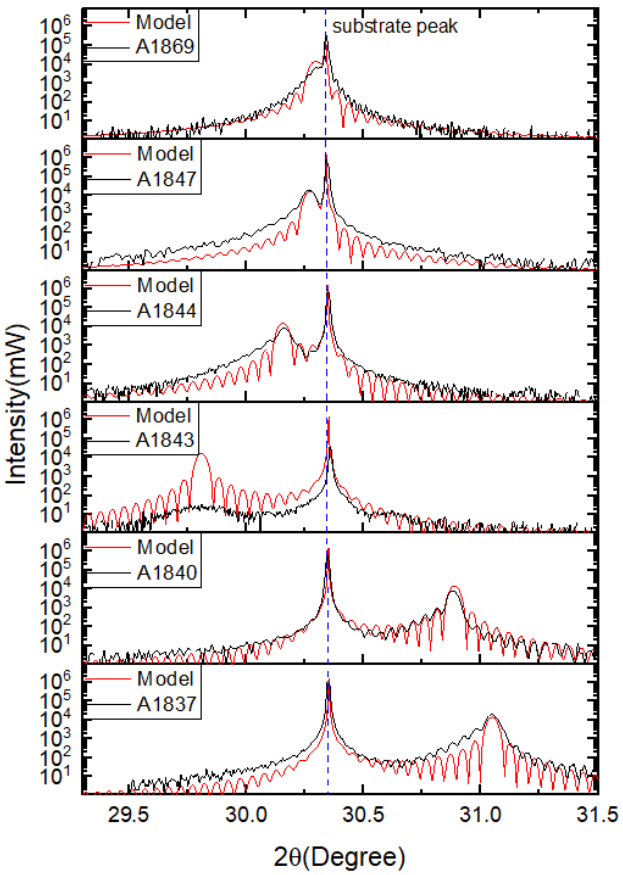

Figure 4.3.2 X-ray diffraction for the four samples of AlInAsSb on InP

Table 4.3.1 X-ray diffraction parameters for the samples of AlInAsSb/InP

Sample No	Structure	Epi angle (°)	Separation (°)	FWHM (')	As%	Thickness(nm)	Epi Intensity	Sub Intensity
A1837	AlInAsSb/GaSb	29.327	0.548	12.480	0.781	1000.000	34.4280	40148.232
A1840	AlInAsSb/GaSb	30.861	0.540	2.520	0.750	1000.000	7825.419	712241.623
A1843	AlInAsSb/GaSb	29.326	0.550	13.200	0.530	1000.000	35.721	39387.586
A1844	AlInAsSb/GaSb	30.181	0.194	2.160	0.604	1000.000	8250.361	912825.512
A1847	AlInAsSb/GaSb	30.268	0.075	3.000	0.628	1000.000	19542.699	766347.079
A1869	AlInAsSb/GaSb	30.294	0.055	4.440	0.632	1000.000	6930.957	350296.149
A1886	1.InGaAlAs/InP	31.497	0.033	1.440	0.250	2000.000	3701.719	308913.019
	2.InGaAlAs/InP	31.569	0.039	2.880	0.850	2000.000	22019.396	

4.4 InGaAs/GaAsSb superlattice (SL) on InP

Four samples of SL were grown by MBE to target strain balanced SL on InP[84]. Each sample was initially grown with an InGaAs buffer layer under conditions similar to those used for the InGaAs layers in the SL. Figure 4.4.1 shows the X-ray diffraction (XRD) patterns of these four samples. Each sample exhibits a set of peaks with the same angular separation, known as satellite peaks, resulting from the periodic structure of the superlattice. The peak adjacent to the InP substrate, referred to as the zeroth-order peak, reflects the strain of the SL relative to the substrate. This peak is close to the substrate peak, indicating no relaxation in the samples; its composition was used for X-ray simulation[85]. The InGaAs buffer layer peak was used to determine the indium composition in InGaAs for the SL simulations. The structural parameters obtained from simulations for each sample are listed in Table 4.4.1. Sample A1792 exhibits a nearly lattice-matched composition. The presence of strong and narrow satellite peaks indicates the high crystalline quality of the superlattices.

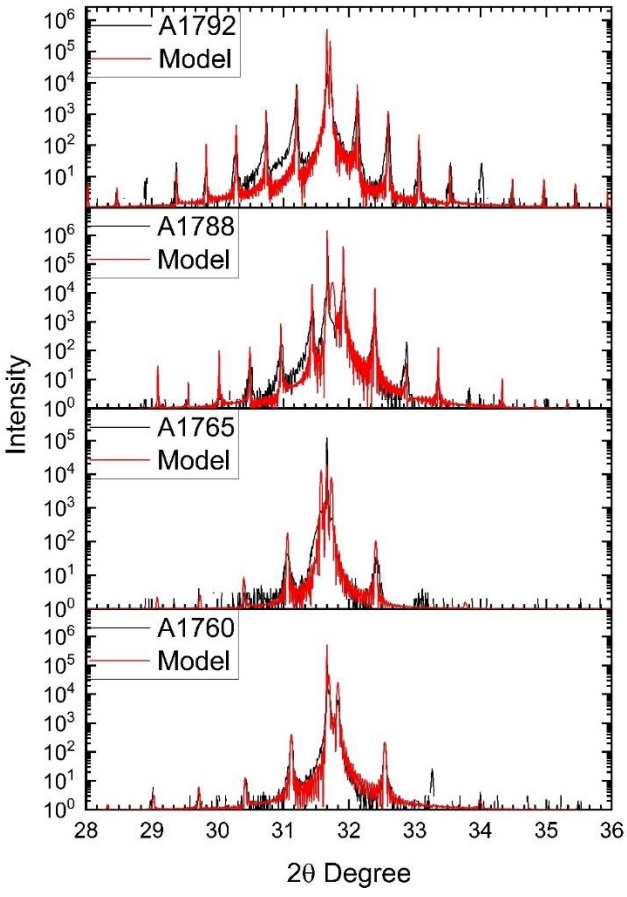

Figure 4.4.1 four samples of InGaAs/GaAsSb SL on InP

Table 4.4.1 Structural details determined from simulation

Sample No	Structure	Sub angle (°)	Epi angle (°)	Separation (°)	In%	As%	GaAsSb Thickness(nm)	InGaAs Thickness(nm)	InGaAs (buffer) Thickness(nm)	Epi Intensity	Sub Intensity
A1760	20x InGaAs/GaAsSb SL on InP	31.721	31.888	0.153	0.525	0.568	4.000	3.289	200.000	6331.261	79490.490
A1765	20x InGaAs/GaAsSb SL on InP	31.543	31.610	0.067	0.550	0.551	4.335	3.382	200.000	506.139	20568.396
A1788	40x InGaAs/GaAsSb SL on InP	31.910	32.155	0.245	0.515	0.587	5.945	4.947	100.000	35152.206	386990.044
A1792	40x InGaAs/GaAsSb SL on InP	31.717	31.665	0.052	0.530	0.451	2.046	9.150	100.000	20132.385	180735.935

4.5 Conclusion

Through optimization of MBE growth, lattice-matched InGaAs, GaAsSb, InGaAs/GaAsSb type-II superlattices (T2SLs) on InP substrates, and InAlAsSb on GaSb substrates were successfully obtained. The X-ray diffraction (XRD) patterns of these lattice-matched alloys exhibit strong and narrow diffraction peaks, demonstrating the high crystalline quality of the materials.

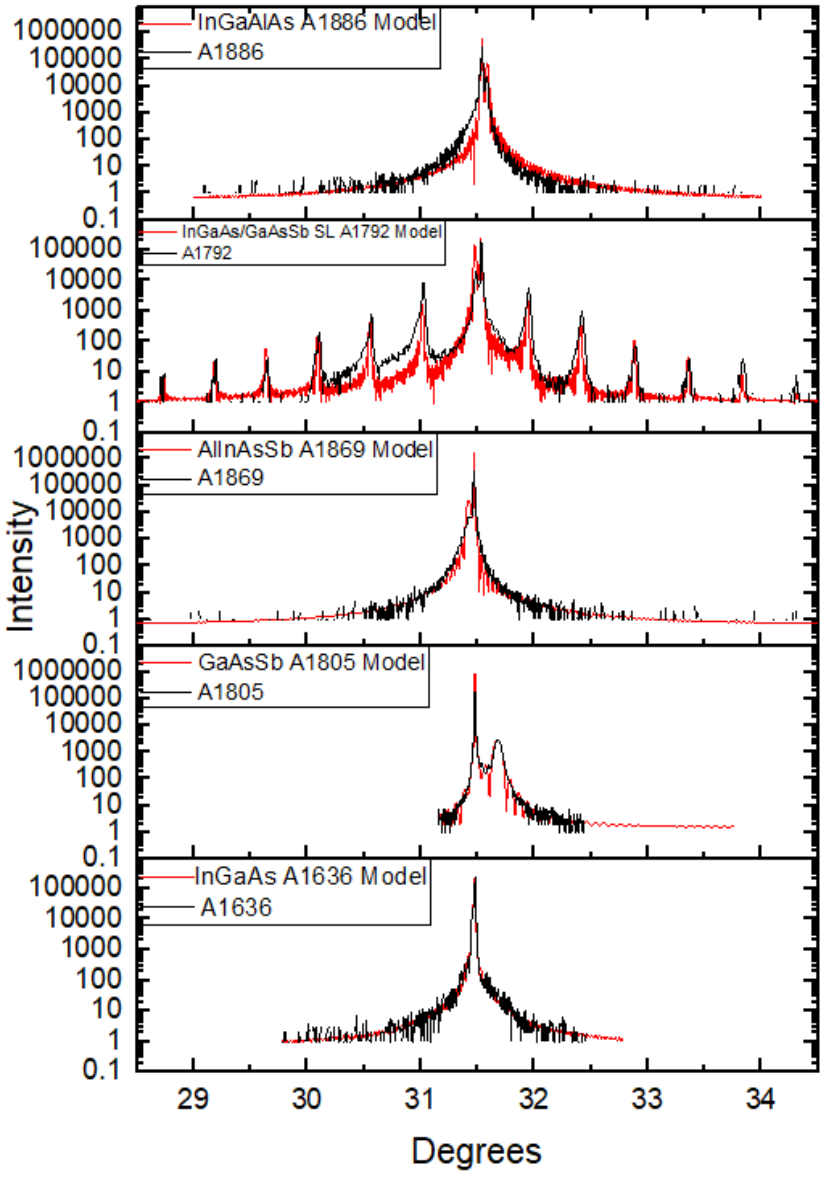

Figure 4.5.1 summary of best samples of devices

Figure 4.5.1 summarizes the X-ray diffraction (XRD) patterns for the best samples of each structure. All of these samples exhibit high-quality crystal growth and structural integrity, representing the best exemplars within their respective material systems. Comparison of the XRD results indicates significant differences in lattice matching and crystalline quality among the different material systems. Although the single-layer InGaAs (A1636) and InGaAlAs (A1886) can be epitaxially grown on the InP substrate, their separation angles are 0.150° and 0.033–0.039°, respectively, indicating a certain degree of lattice mismatch. Furthermore, due to the thick epitaxial layers, strain relaxation and defects can be introduced into the structures [86]-[87]. Similarly, the single-layer GaAsSb (A1805) and AlInAsSb (A1869) were successfully epitaxially grown on the substrate, but their separation angles of 0.200° and 0.055° still indicate lattice mismatch. Moreover, their satellite peaks are poorly resolved, reflecting insufficient periodicity and interface flatness[88]-[89]. In contrast, the InGaAs/GaAsSb superlattice (A1792) is well lattice-matched to InP, with a separation angle of only 0.052°. In addition, the satellite peaks of A1792 are well resolved, indicating a highly controllable superlattice period, flat interfaces, and higher crystalline quality than the other samples[90]. Therefore, based on the XRD data, the A1792 InGaAs/GaAsSb superlattice demonstrates the best lattice matching and structural integrity, making it an optimal candidate for the growth of e-SWIR photodetectors with a 2.5 μm-thick T2SL absorption layer.

Chapter 5 Photoluminescence (PL) Studies

To investigate the optical properties of semiconductor materials lattice-matched to InP, including InGaAs, GaAsSb, InAlAsSb, and InGaAs/GaAsSb type-II superlattices (T2SLs), a 650 nm laser was used to excite the samples with powers ranging from 20 to 140 mW. Photoluminescence (PL) measurements were also performed at various temperatures, ranging from 8 K to 300 K. Table 5.1 summarizes the samples studied in this work.

Table 5.1. summary of samples

Sample No	Structure	Thickness(nm)
A1597	$In_{0.55}Ga_{0.45}As$ on InP	211.500
A1636	$In_{0.54}Ga_{0.46}As$ on InP	211.400
A1805	$GaAs_{0.55}Sb_{0.45}$ on InP	240.000
A1840	$Al_{0.3}InAs_{0.75}Sb$ on GaSb	108.860
A1869	$Al_{0.3}InAs_{0.63}Sb$ on GaSb	274.500
A1788	$In_{0.52}GaAs/GaAs_{0.59}Sb$ SL on InP	1000.000
A1792	$In_{0.53}GaAs/GaAs_{0.45}Sb$ SL on InP	1000.000

5.1 InGaAs

Two 200 nm InGaAs epilayer samples on InP were studied: A1597, with an indium content of 0.55 (determined by X-ray, corresponding to a lattice mismatch of +0.018), and A1636, with an indium content of 0.54, nearly lattice-matched to InP. In general, the lattice mismatch of InGaAs with InP strongly influences both structural and optical properties[91]-[92]. Figure 5.1.1 shows the 8 K photoluminescence (PL) spectra at various laser excitation powers. Two peaks were observed for both samples: the left peak originates from the InGaAs epilayer, while the right peak corresponds to the second-order peak from the InP substrate. The indium composition can be calculated from the peak wavelength. For A1597, the PL peak at 1559.30 nm indicates an indium composition of 0.55, while A1636, with a peak at 1542.67 nm, corresponds to an indium composition of 0.54. These results are consistent with the compositions determined by X-ray diffraction. The intensity and full width at half maximum (FWHM) of the two samples are summarized in Table 5.1.1.

To assess the material quality, power-dependent PL measurements were performed on the samples. The emission peaks are centered at 1559.30 nm for A1597 and 1542.67 nm for A1636, remaining unchanged as the laser excitation power increases, indicating that the emission arises from band-to-band transitions rather than defect-related states[93]. Moreover, the PL intensity increases monotonically with laser power, a characteristic of efficient radiative recombination in high-quality InGaAs epilayers. The PL data of the samples are summarized in Table 5.1.1.

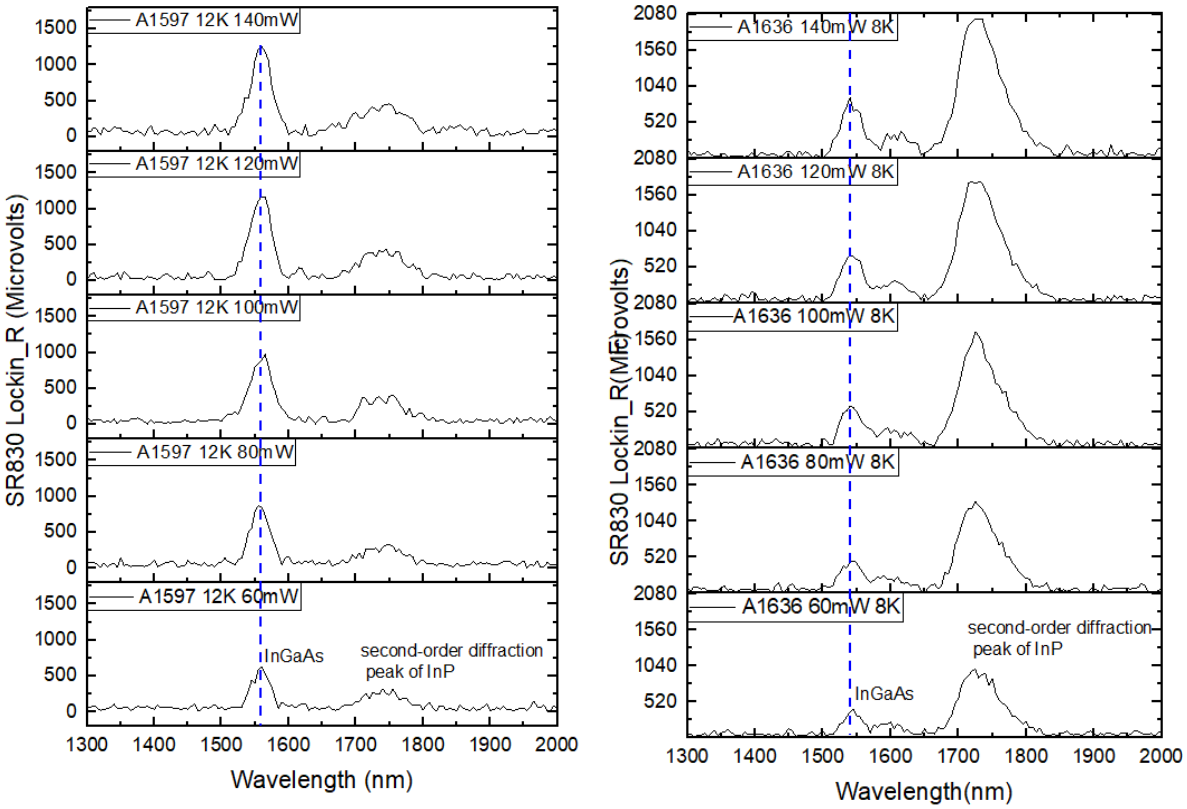

Figure 5.1.1PL for sample A1597, A1636 for InGaAs

Table5.1.1 PL parameters for sample A1597, A1636 of InGaAs

Sample No	Thickness (nm)	Peak wavelength (nm)	Intensity	FWHM (nm)
A1597	211.500	1559.297	1253.140	32.462
A1636	211.400	1542.672	875.477	34.000

5.2 GaAsSb

One 200 nm GaAsSb epilayer sample on InP, A1805, was studied, with an arsenic composition of 0.55, resulting in a lattice mismatch of +0.04. Figure 5.5 shows the 8 K photoluminescence (PL) spectra at various laser excitation powers. Two peaks were observed for this sample: the left peak originates from the InP substrate, while the right peak, centered at 1750.62 nm, is attributed to the GaAsSb epilayer.

The arsenic composition was estimated from the dependence of the bandgap on arsenic content (see Equation 2.1.1). The lowest bandgap is 0.777 eV at an arsenic composition of 0.179. The observed PL emission energy is lower than this value, indicating that the emission does not originate from the GaAsSb epilayer. The lower-energy emission likely arises from type-II transitions of photo-generated carriers at the InP/GaAsSb interface, as illustrated in Figure 5.2.1. The PL intensity and full width at half maximum (FWHM) of this sample are summarized in Table 5.2.2.

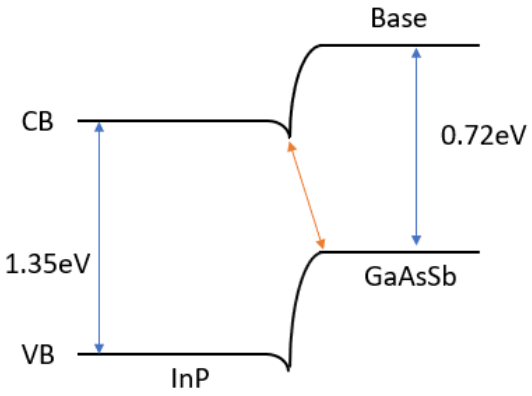

Figure 5.2.1 band diagram GaAsSb/InP bandgap alignment

To assess the material quality, power-dependent photoluminescence (PL) measurements were performed on the sample. The emission peak was observed to be centered at 1750.62 nm and remained unchanged as the laser excitation power increased, indicating that the emission originates from band-to-band transitions. Moreover, the emission peak intensity was observed

to increase with increasing laser excitation power, consistent with efficient radiative recombination in the material.

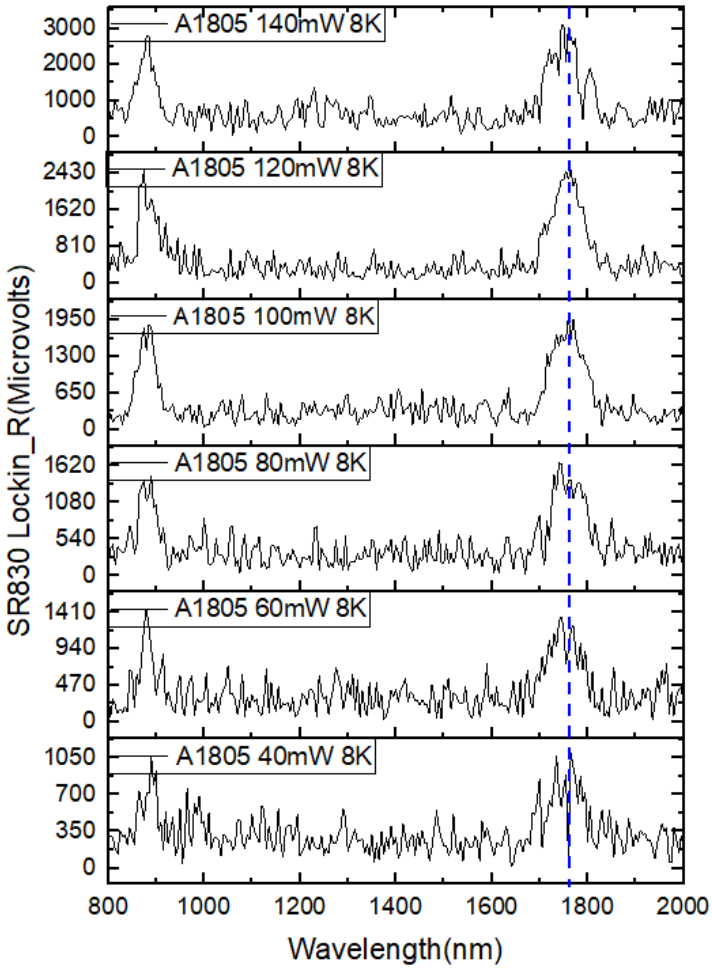

Figure 5.2.2 PL for sample A1805 for GaAsSb

Table 5.2.1 PL parameters of sample A1805 for GaAsSb

Sample No	Thickness(nm)	Peak wavelength(nm)	Intensity	FWHM (nm)
A1805	240.000	1750.621	3122.340	87.525

5.3 AlInAsSb

Two InAlAsSb epilayer samples on GaSb, with thicknesses of 108.86 nm (A1840) and 274.50 nm (A1869), were studied. A1840 has an arsenic composition of 0.75, resulting in a lattice mismatch of +0.109, while A1869 has an arsenic composition of 0.63, nearly lattice-matched to GaSb. Figure 5.3.1 shows the 8 K photoluminescence (PL) spectra of A1840 at various laser excitation powers. The left peak originates from the InP substrate, while the right peak is attributed to the InAlAsSb epilayer. Figure 5.3.2 shows the PL spectrum of A1869, which exhibits a single peak originating from the InAlAsSb epilayer.

The arsenic composition was estimated from the peak wavelengths using the bandgap dependence on arsenic composition (see Equation 2.1.1). For A1840, the PL peak at 2380.67 nm corresponds to an arsenic composition of 0.632, while A1869, with a peak at 2382.49 nm, corresponds to an arsenic composition of 0.631. These results are consistent with the compositions determined by X-ray diffraction.

To assess the material quality, power-dependent PL measurements were performed on both samples. The emission peaks were centered at 2380.67 nm for A1840 and 2382.49 nm for A1869. A slight blue shift of the peak wavelengths was observed with increasing laser excitation power, indicating the presence of recombination through localized states arising from compositional nonuniformity[94]. Temperature-dependent PL measurements were also performed. A1840 quenched above 20 K, while A1869 quenched above 30 K, reflecting the improved lattice matching of A1869 and highlighting the importance of lattice-matched epilayers for high-performance devices. The PL intensity and full width at half maximum (FWHM) of the samples are summarized in Table 5.3.1.

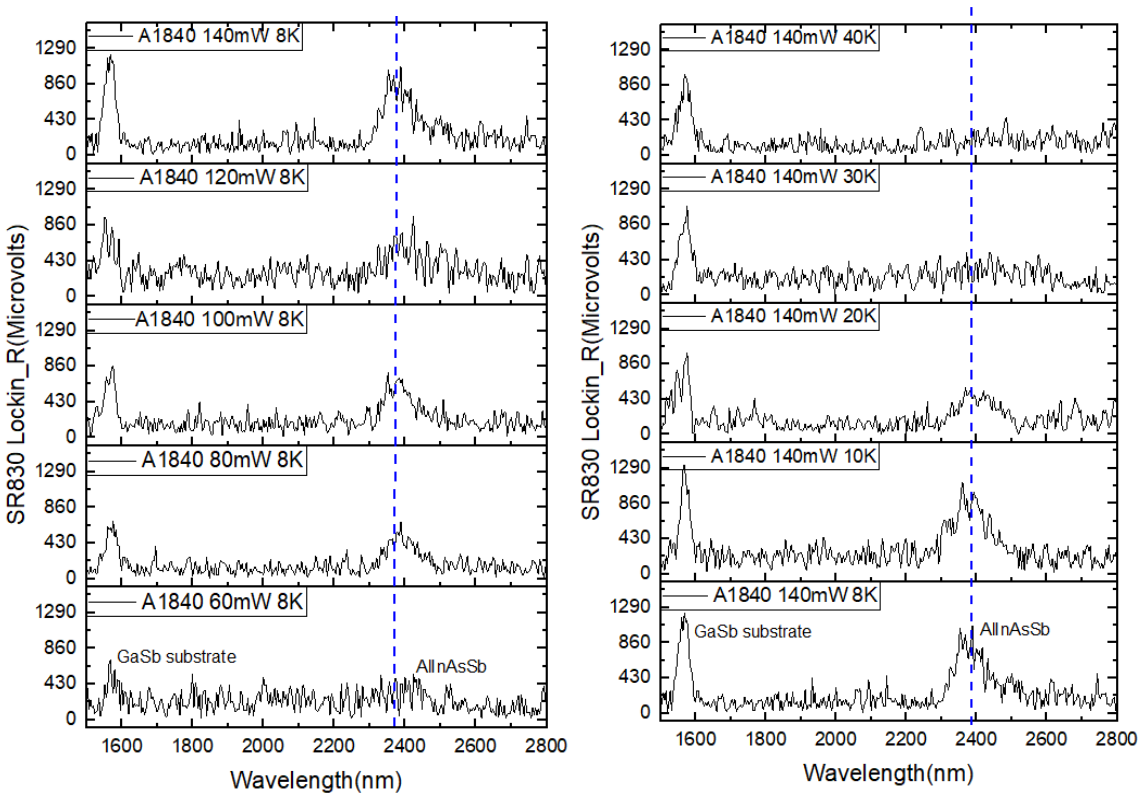

Figure 5.3.1 PL for sample A1840 for AlInAsSb

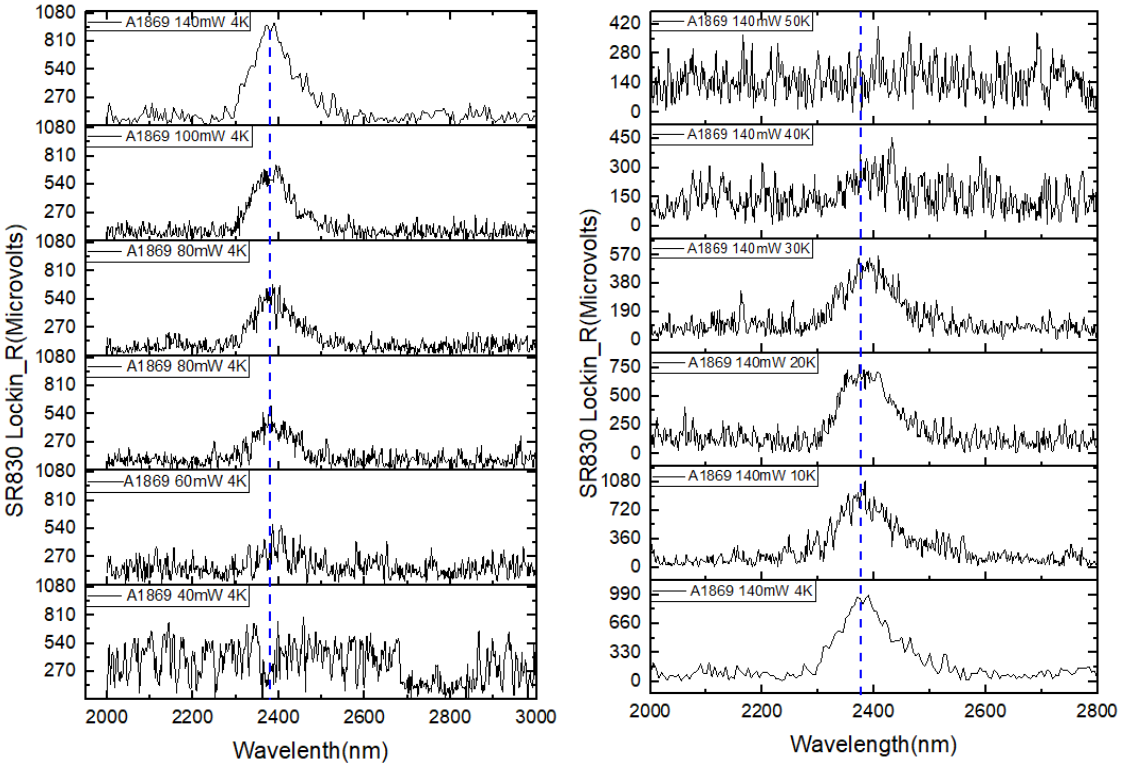

Figure 5.3.2 PL for sample A1869 for AlInAsSb

Table 5.3.1 PL parameters of sample A1805 for AlInAsSb

Sample No	Thickness(nm)	Peak wavelength(nm)	Intensity	FWHM (nm)	T_{max} (K)
A1840	108.864	2380.671	770.573	99.093	20.000
A1869	274.500	2382.491	946.049	96.790	40.000

5.4 SL

Two InGaAs/GaAsSb (4.5 nm/4.5 nm) type-II superlattice (T2SL) samples, with a thickness of 1000 nm, were studied on InP (see Section 4.4 for detailed structures). A1788 has InGaAs with an indium content of 0.52 (lattice mismatch of +0.01) and GaAsSb with an arsenic content of 0.59 (lattice mismatch of 0.07), while A1792 has InGaAs with an indium content of 0.53 (nearly lattice-matched) and GaAsSb with an arsenic content of 0.45 (lattice mismatch of +0.061). Figure 5.4.1 shows the 8 K photoluminescence (PL) spectra at various laser excitation powers. Three peaks were observed for both samples: the left peak originates from the InGaAs buffer layer, the middle peak corresponds to the third-order laser line (650 nm), and the right peak originates from the T2SL layer, which is the main focus of this study.

The indium composition was estimated from the T2SL emission peak wavelength. For A1788, the peak at 2157.69 nm indicates an indium composition of 0.55, while A1792, with a peak at 2137.27 nm, corresponds to an indium composition of 0.54. These results are consistent with the compositions determined by X-ray diffraction.

To assess the material quality, power-dependent PL measurements were performed on both samples. A pronounced blue shift of the T2SL emission peak was observed for both samples as the laser excitation power increased, which is a typical behaviour of type-II band alignment quantum structures[95]-[96] . Meanwhile, the emission peak intensity was observed to increase with increasing laser excitation power.

.

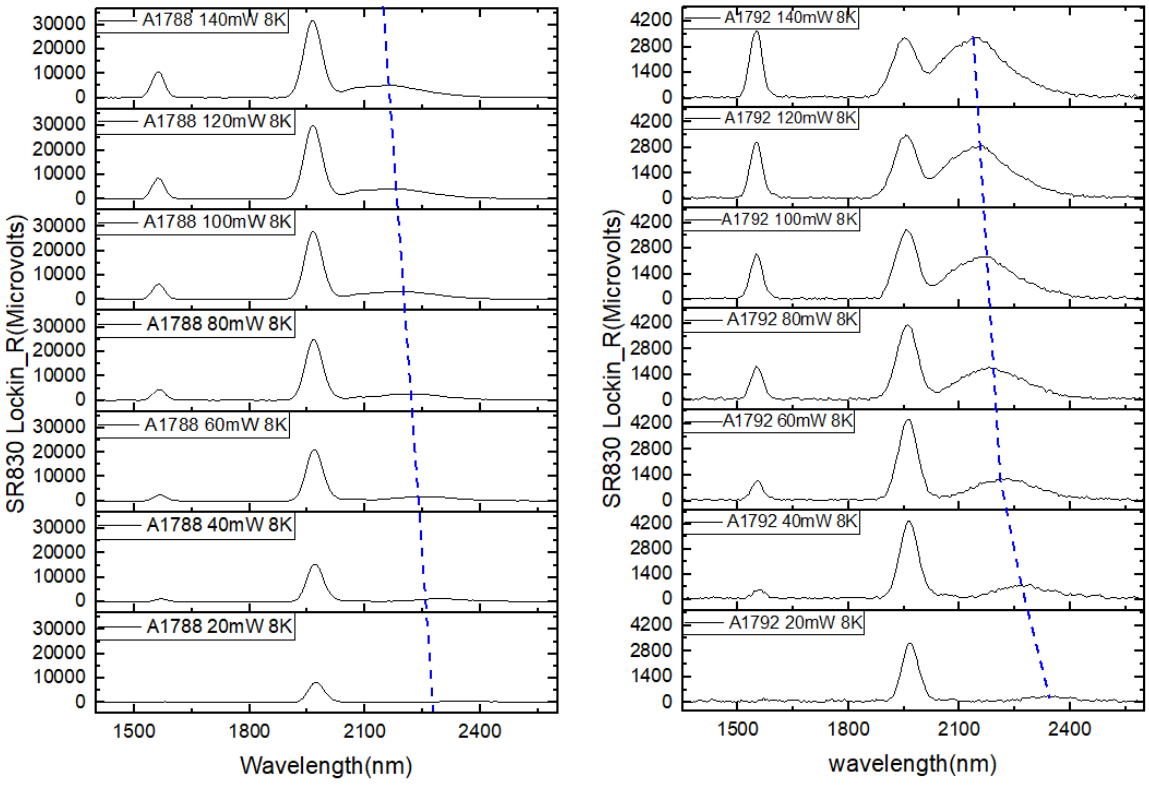

Figure 5.4.1 PL for sample A1788, A1792 for InGaAs/GaAsSb SL

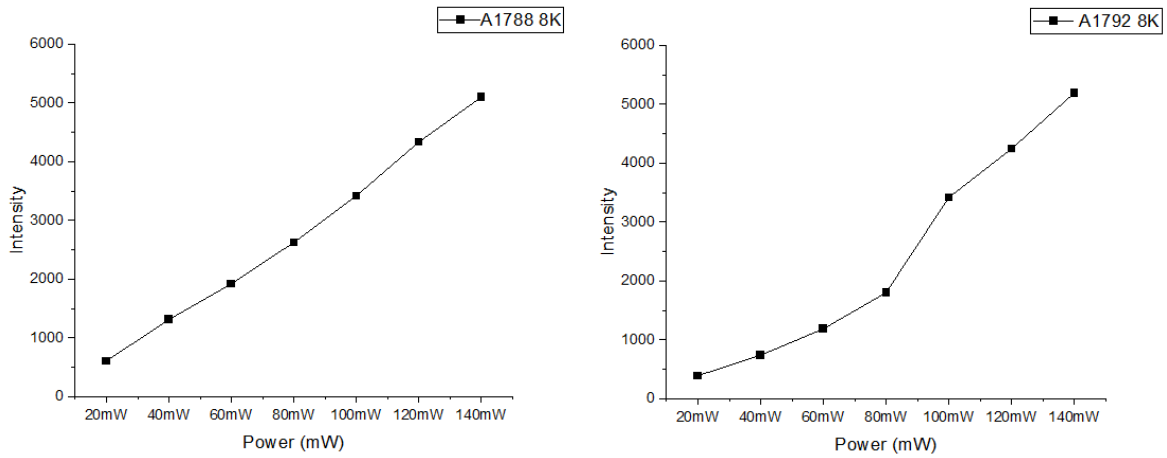

(a) (b)

Figure 5.4.2 Power-dependent PL Intensity for A1788 (a) and A1792 (b)

Figure 5.4.2(a) shows the power-dependent photoluminescence (PL) intensity characteristics of samples A1788 and A1792 at 8 K. Overall, as the excitation power increased from 20 mW to 140 mW, the PL intensity of both samples exhibited a continuous increase, indicating efficient optical responses. The PL intensity of A1788 increased approximately linearly with increasing excitation power, suggesting a stable carrier recombination process and high radiative recombination efficiency. In contrast, the PL intensity of A1792 increased gradually in the low-power region (20–80 mW), but showed a pronounced increase above 100 mW, indicating that the carrier recombination mechanism may be influenced by filling of localized states or saturation of defect states at high excitation power, thereby enhancing the radiative recombination efficiency. Overall, A1788 exhibited a more uniform and predictable response, while the pronounced intensity enhancement of A1792 at high power indicated higher luminescence potential under strong excitation conditions.

Figure 5.4.2 shows the dependence of the T2SL photoluminescence (PL) emission peak on laser excitation power. For sample A1788, a blue shift from 2368 nm to 2158 nm and a broadening of the full width at half maximum (FWHM) from 164 nm to 252 nm were observed. In contrast, A1792 exhibited a blue shift from 2343 nm to 2137 nm, with FWHM broadening from 150 nm to approximately 300 nm. Peak blue shift is a typical behavior of type-II band-aligned quantum structures and has been observed in many type-II superlattices, such as InAs/GaSb [97]. This blue shift is primarily attributed to band bending and the reduced spatial separation between electron and hole wavefunctions under high optical excitation, which enhances Coulomb interactions and increases the transition energy[98]. These observations confirm that the superlattices grown in this work exhibit type-II band alignment. The broadening of the PL peak FWHM is associated with inhomogeneities in well thickness and composition, carrier–carrier scattering, and band-filling effects under strong optical pumping[99]. The PL features of T2SL were summarised in table 5.4.1.

Table 5.4.1 PL parameters of sample A1788, A1792 for InGaAs/GaAsSb SL

Sample No	Thickness(nm)	Peak wavelength(nm)	Intensity	FWHM (nm)
A1788	1000.000	2157.691	5096.471	251.592
A1792	1000.000	2137.268	5188.020	269.894

5.5 APD

Owing to advances in type-II superlattices (T2SLs), we investigated their potential for avalanche photodiode (APD) applications. To support this study, photoluminescence (PL) measurements were performed on a set of APD devices. Sample A1902 is an InGaAs/GaAsSb T2SL APD wafer grown on an InP substrate. The APD structure consists of an n-InGaAs barrier layer, multiple layers of AlGaAsSb serving as the multiplication and charge layers, followed by a thin InGaAlAs transition layer, 188 pairs of 5 nm/5 nm InGaAs/GaAsSb T2SL absorber layers, and a top contact layer composed of thick, heavily doped InGaAs. Sample A1908 is an InGaAs APD with the same structure as A1902, except that the absorber is replaced by InGaAs.

Figure 5.5.1(a) shows the 5 K PL spectra of A1902 at various laser excitation powers. Two peaks were observed: the left peak originates from the InGaAs buffer layer, while the right peak corresponds to the InGaAs/GaAsSb T2SL absorption layer. The PL intensity of both peaks increased with excitation power, and the emission wavelengths were blue-shifted slightly, consistent with behaviours observed in previous studies[100]-[101].

Figure 5.5.1(b) shows the temperature-dependent PL of A1902. At low temperatures (5 K), the T2SL emission peak appears at approximately 2200 nm (0.564 eV). As the temperature increases to 150 K, the peak blue-shifts to approximately 2050 nm (0.605 eV), followed by a slight red-shift up to 200 K. The PL peak exhibits an "S-shaped" temperature dependence, indicating that carrier localization dominates luminescence at low temperatures [102], As the sample is heated, these carriers delocalize and recombine at higher-energy states until complete delocalization occurs, as described by phenomenological models for exciton localization[103]. At higher temperatures, the intrinsic bandgap shrinkage of the material becomes the dominant effect[104]. At the same time, the luminous intensity rapidly decreases and thermal quenches during the further heating process[105].

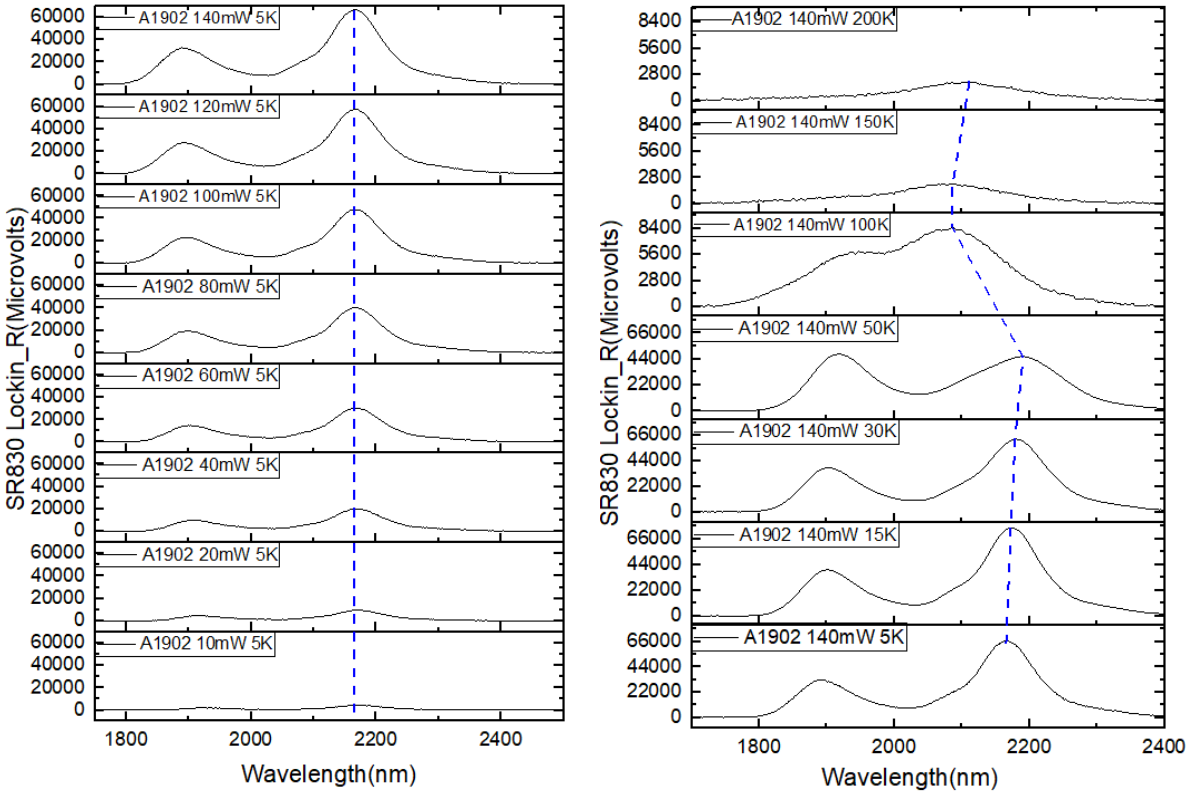

(a) (b)

Figure 5.5.1 PL for sample A1902 InGaAs/GaAsSb T2SL APD at varied laser excitation power and 5 K (a) (5K), and varied temperature of 5K to 200K with laser excitation power of 140 mW.

5.6 Conclusion

The major PL features of all the samples are summarized in Table 5.4.2. It can be seen that all samples grown under optimized growth conditions exhibit efficient emission, except for GaAsSb/InP, where luminescence is dominated by type-II interface recombination. Importantly, to achieve long-wavelength operation for e-SWIR photodetectors, both T2SL and AlInAsSb materials can be employed. However, T2SL exhibits a much stronger emission intensity, indicating its superior optical quality. Although its FWHM is wider than that of AlInAsSb, this is expected to enable a broader spectral response. Consequently, in this study, T2SL was employed as the absorber for e-SWIR photodetectors.

Furthermore, PL measurements on a T2SL APD revealed a strong emission with an intensity of 32,690. and a peak wavelength of 2165 nm, indicating the high quality of the absorber. This further confirms the suitability of T2SL for e-SWIR photodetector applications.

Table 5.6.1 PL summary of samples

Sample No	Structure	T(K)	Laser power (mW)	λ_p (nm)	FWHM (nm)	Intensity
A1597	InGaAs on InP	8.000	140.000	1750.000	94.456	455.858
A1636	InGaAs on InP	8.000	140.000	1731.004	65.258	2004.640
A1805	GaAsSb on InP	8.000	140.000	1750.621	87.525	3122.340
A1788	InGaAs/GaAsSb T2SL on InP	8.000	140.000	2149.159	251.592	5096.470
A1792	InGaAs/GaAsSb T2SL on InP	8.000	140.000	2153.558	269.894	5188.020
A1840	AlInAsSb on GaSb	8.000	140.000	2380.671	99.093	770.573
A1869	AlInAsSb on GaSb	8.000	140.000	2382.491	96.790	946.049
A1902	InGaAs/GaAsSb T2SL APD	8.000	140.000	2165.504	65.418	5075.723

Chapter 6 T2SL nBp e-SWIR photodetector

Based on the calibrated InGaAs/GaAsSb T2SL grown on InP substrates, an nBp device structure was designed for wavelength-extended near-infrared photodetector applications. Several device wafers were grown through multiple growth attempts. The best-performing wafers were subsequently fabricated into mesa-structured infrared photodetectors, and their I–V characteristics and detection performance were systematically investigated.

6.1 Design, growth and fabrication of T2SL e-SWIR photodetector

Molecular beam epitaxy (MBE) was employed in this study to grow nBp detector epitaxial structures on InP substrates. MBE is a non-equilibrium epitaxial growth technique operated under ultra-high vacuum conditions, in which the growth process is primarily governed by surface kinetic mechanisms. Group III elements (In, Ga, and Al) were supplied from solid-state effusion cells, while group V elements (As and Sb) were provided as diatomic molecular beams using valved cracker sources. By precisely controlling the substrate temperature, group III/V flux ratio, and the opening and closing of source shutters, the thickness, composition, and heterointerface abruptness of the epitaxial layers were accurately controlled. This level of control is critical for the realization of high-quality InGaAs/GaAsSb superlattice absorption layers and AlGaAsSb barrier layers.

The molecular beam fluxes were calibrated using beam equivalent pressure (BEP), and surface reconstruction and growth kinetics were monitored in situ by reflection high-energy electron diffraction (RHEED). The excellent controllability and high-quality interface characteristics of solid-source MBE make it particularly suitable for the epitaxial growth of multilayer InGaAs/GaAsSb/AlGaAsSb nBp heterostructures investigated in this work.

The schematic structure of the nBp detector is shown in Figure 6.1(a). After the deposition of a 0.5 μm n-InGaAs bottom contact layer, 200 pairs of InGaAs/GaAsSb absorber layers with individual thicknesses of 5 nm/5 nm were grown. This was followed by the deposition of a 5 nm-thick $Al_{0.35}GaAsSb$ barrier layer. The structure was finally capped with a 100 nm-thick heavily p-doped GaAsSb layer serving as the top contact layer. The corresponding band diagram of the nBp structure is illustrated in Figure 6.1(b). The AlGaAsSb layer, which is lattice

matched to the InP substrate, acts as an energy barrier to suppress diffusion current, thereby reducing the dark current of the device. The grown wafer was then fabricated to standard mesa-structured photodetector devices at various mesa sizes by standard photolithography process. The mesa was dry-etched by an inductive coupled plasma (ICP) instrument, followed by metallisation of Ti/Au to the contact layers for bottom and top contacts, then finalised by deposition of a 200 nm thick SiO_2 layer for passivation. The devices were primarily investigated by looking at I-V characteristics over various temperatures. The best devices were then selected for spectral photoresponse study at room temperature.

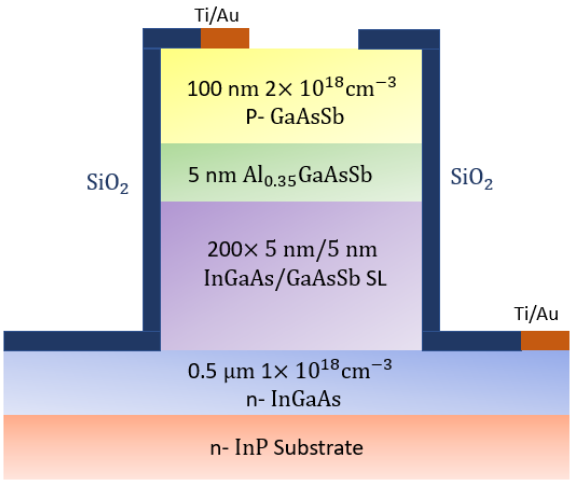

(a)

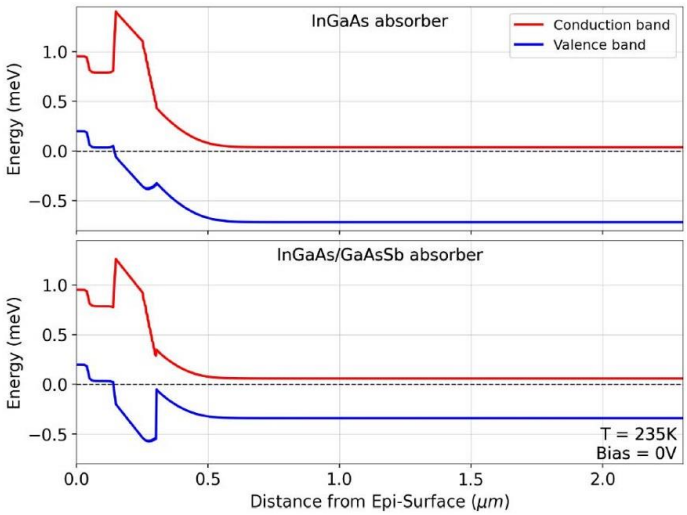

(b)

Figure 6.1.1 Schematic diagram of the T2SL nBp e-SWIR photodetector (sample A1769) (a) and the bandgap diagram of the device (b)

6.2 Structural analysis of the T2SL nBp photodetectors

Figure 6.2.1 shows the XRD scan test and the fitting of sample A1769. The XRD scan shows large number of sharp and intense satellite peaks of the sample the 0^{th}-order peak close to the InP substrate, indicating a low lattice mismatch of the T2SL and the high crystalline quality and abrupt interfaces. The peaks of bottom InGaAs layer and top GaAsSb layer are also visible. The simulation reveals the actual structure is $In_{0.535}GaAs$, $In_{0.535}GaAs/GaAs_{0.5}Sb$ T2SL, $Al_{0.35}GaAs_{0.5}Sb$, and $GaAs_{0.511}Sb$. The overall results show that the epitaxial growth structure is close to the designed structure in terms of layer thickness, composition control, and superlattice interfaces control. Owing to its high crystalline quality, we processed this wafer into mesa-structured diodes to evaluate feasibility for e-SWUR infrared detection.

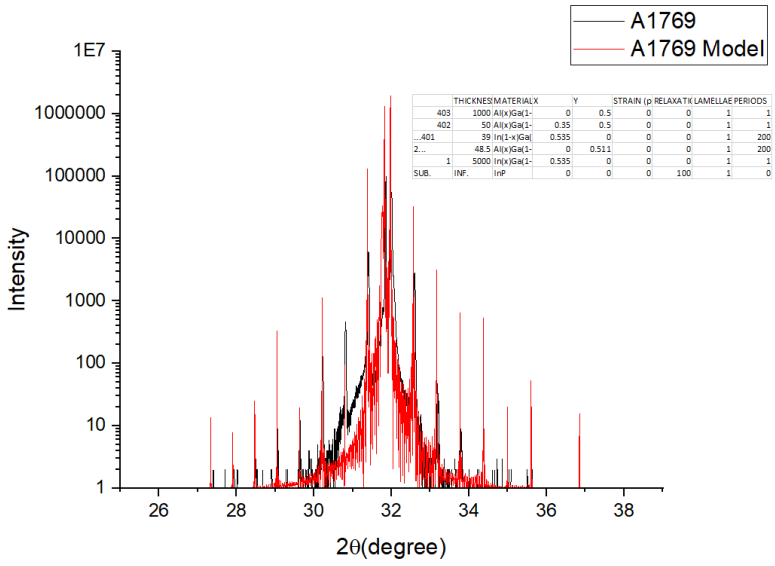

Figure 6.2.1 X-ray of A1769

6.3 IV measurements

The I–V characteristics of devices with a mesa diameter of 0.8 mm were measured using a home-built probe station. Figure 6.3.1 shows the I–V curves of six representative devices. All devices exhibit clear asymmetric I–V behaviour, characterized by very low dark current under reverse bias and an exponentially increasing current under forward bias. Under a reverse bias

of –2 V, the devices show dark current densities in the range of 2–20 mA/cm², which are relatively low. It should be noted that variations in dark current are observed among different devices. These variations may originate from material nonuniformity in the epitaxial growth or from process-induced variations during device fabrication.

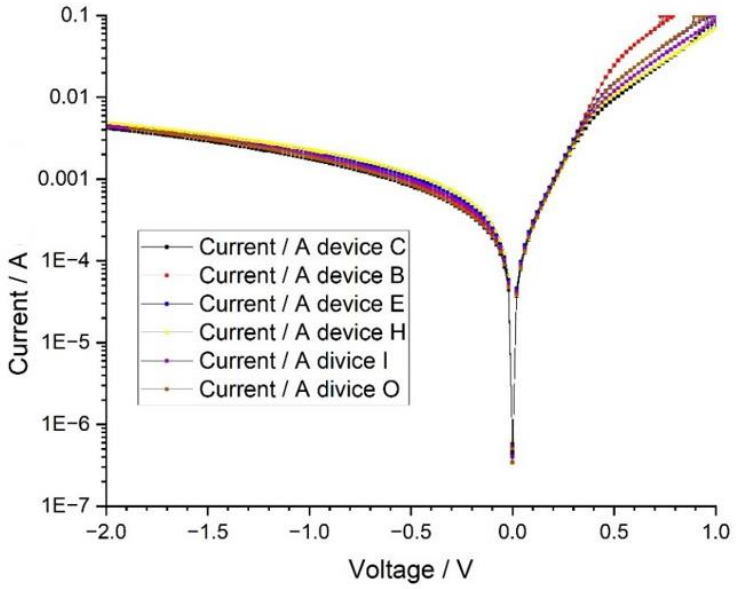

Figure 6.3.1 IV characteristic of T2SL nBp photodetector (A1769)

Figure 6.3.2 shows the dark I-V characteristic curve of the A1769 device over the range of 12 K to 300 K. It can be observed that the device exhibits a reduced dark current when the temperature reduces. An ultra-low dark current of 10^{-8} A at reverse bias of –1 V can be obtained at 12 K, indicating that the defect-assisted tunnelling process and surface leakage current are effectively suppressed. This is typically observed in pin structures. As the temperature increases, the dark current gradually increases, mainly due to the generation-recombination process of thermal activation, the enhancement of diffusion current and the increased surface leakage current. At room temperature (300 K), the device's dark current at 1 V reverse bias is maintained in the range of 10^{-4}–10^{-3}A, which is lower compared to some reported Type II superlattice photodiodes, demonstrating the advantages of the nBp structure in reducing dark current by using the AlGaAsSb barrier and the success of MBE growth of the high crystalline quality and strain-compensated overall structure. It is worth noting that,

throughout the temperature range, the I–V curves of the devices show a strong asymmetry under the forward and negative deviations, which further indicates that the high quality of the p-n junction.

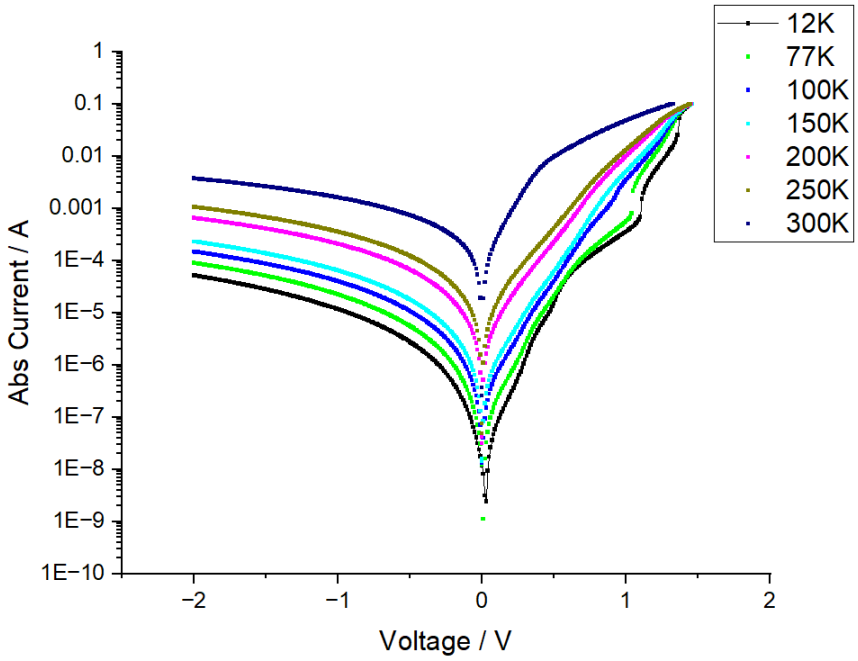

Figure 6.3.2 Temperature varied IV characteristics for T2SL nBp e-SWIR photodetector A1769 H.

6.4 Spectral photoresponse

To measure the spectral photoresponse of the InGaAs/GaAsSb T2SL e-SWIR photodetectors, a Thorlabs SLS202 broadband light source was used to illuminate the devices in a photoresponse measurement setup adapted from the photoluminescence system. All measurements were performed at room temperature. For performance benchmarking, the measured photoresponse was compared with that of a commercial Thorlabs photodetector.

Figure 6.4.1 shows the spectral photoresponse of six devices fabricated from wafer A1769. All devices exhibit a photoresponse over the wavelength range from 750 nm to approximately 2250 nm, beyond which no measurable response is observed. The peak responsivity is located in the wavelength range of 1000–1500 nm. The cutoff wavelength of approximately 2250 nm

is consistent with the photoluminescence emission peak at around 2200 nm, confirming that the photoresponse originates from the InGaAs/GaAsSb T2SL absorber.

Significant variations in photoresponse are observed among different devices. These variations are attributed to device nonuniformity introduced during fabrication, as well as possible material nonuniformity across the epitaxial wafer. The effective spectral response bandwidth of these devices is approximately 1338 nm. The best-performing device exhibits a peak photoresponse signal of approximately 30 mV at a wavelength of 1500 nm. Notably, this value is substantially higher than the peak photoresponse of approximately 2.4 mV measured from a commercial Thorlabs SM05PD5A photodetector, which employs lattice-matched InGaAs as the absorber. This comparison highlights the promising performance potential of the InGaAs/GaAsSb T2SL e-SWIR photodetectors developed in this work.

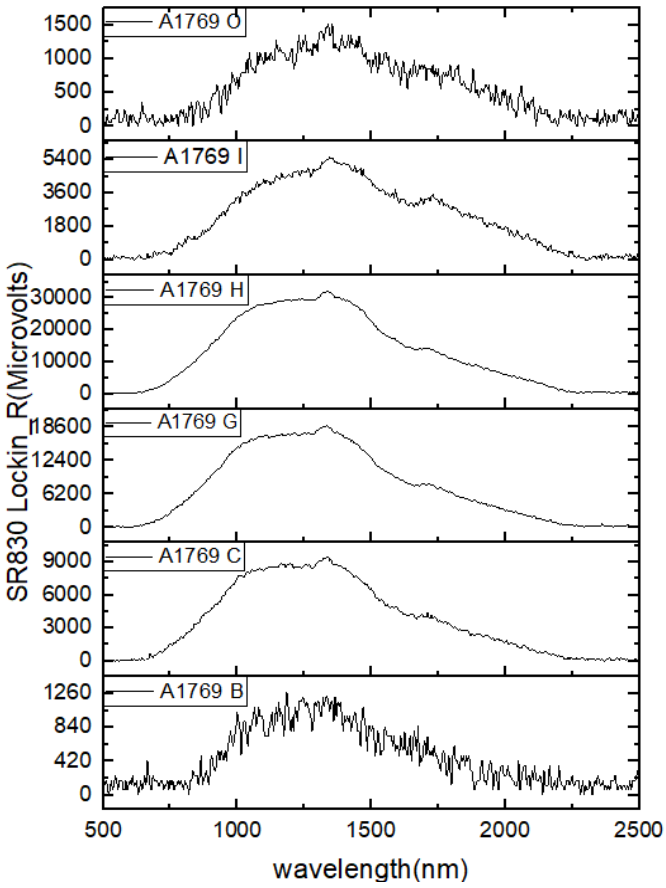

Figure 6.4.1 six samples of InGaAs/GaAsSb SL on InP device (A1769)

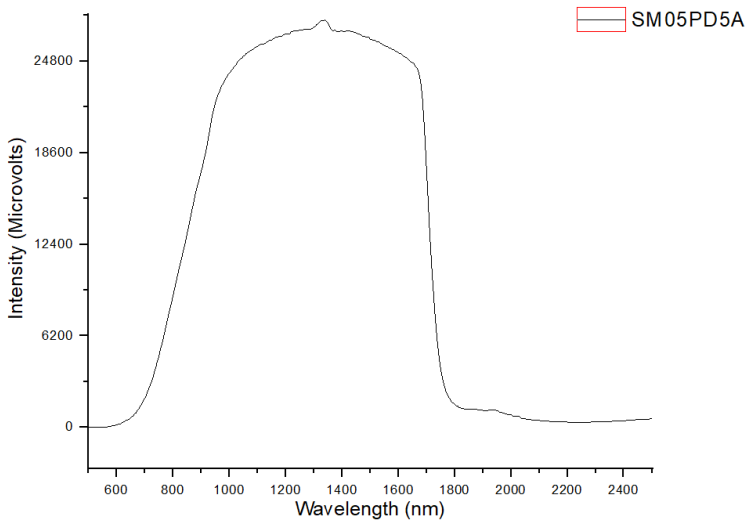

Figure 6.4.2 Spectral photoresponse of commercial device SM05PD5A

6.5 Conclusion

This chapter systematically investigated the design, epitaxial growth, device fabrication, and performance of InGaAs/GaAsSb T2SL-based nBp e-SWIR photodetectors on InP substrates. High-resolution X-ray diffraction (HRXRD) scans and simulations confirmed the successful molecular beam epitaxy (MBE) growth of the designed structure for sample A1769, exhibiting high crystalline quality and abrupt superlattice interfaces.

I–V characterization of devices with a mesa diameter of 0.8 mm shows low leakage current densities in the range of approximately 2–20 mA/cm² under a –2 V reverse bias. Temperature-dependent I–V measurements indicate that the dark current decreases to less than 10^{-8} A at low temperatures. Spectral photoresponse measurements reveal that the A1769 device exhibits a broad photoresponse spanning 600–2250 nm, with a cutoff wavelength of 2250 nm, consistent with the photoluminescence emission wavelength of approximately 2200 nm. The peak responsivity occurs in the wavelength range of 1000–1500 nm, confirming that the absorbing layer is indeed the InGaAs/GaAsSb superlattice.

The photoresponse of the A1769 device was compared with a commercial SWIR photodetector based on indium-rich InGaAs (Thorlabs SM05PD5A, active area 0.5 mm²). The results indicate that the T2SL device exhibits higher responsivity, highlighting its potential as a promising

candidate for extended-wavelength infrared photodetection. In summary, the A1769 device demonstrates low dark currents and strong spectral response, underscoring its potential advantages for high-sensitivity e-SWIR detection applications.

Chapter 7 Conclusion and future work

In this thesis, we systematically investigate the design, growth, structural characterization, and performance of InGaAs/GaAsSb Type II (T2SL) e-SWIR detectors on InP substrates. Through MBE optimization, we successfully achieved lattice-matched epitaxy of InGaAs, GaAsSb, and InGaAs/GaAsSb T2SL on InP substrates, with InGaAs/GaAsSb T2SL exhibiting the best lattice matching and interface quality. PL tests show that T2SL exhibits stronger luminescence, longer emission wavelengths, and better optical quality than AlInAsSb, making it suitable as an absorber material. Based on this, we fabricated a T2SL light detector (A1769) with an nBp structure, whose XRD results indicate abrupt interfaces and high crystalline quality.

Device testing shows that the detector exhibits a dark current density of only 2–20 mA/cm² at –2 V reverse bias and can reduce the dark current to below 10^{-8} A at low temperatures, demonstrating excellent suppression of defect-related tunnelling current. Spectral response measurements show that the device covers a wide spectral range of 600–2250 nm, with a cut-off wavelength around 2250 nm, consistent with PL emission, and exhibits a strong peak response in the 1000–1500 nm range. The A1769 demonstrates a broader response range and higher response intensity compared to commercial indium-rich InGaAs devices, highlighting its potential for high-sensitivity e-SWIR detection.

Although the design, growth, and implementation of the InGaAs/GaAsSb T2SL e-SWIR detector have been successfully completed in this thesis, several directions remain for further optimization. First, in device design, carrier collection efficiency can be enhanced and leakage current further suppressed through optimization of the nBp structure. Second, while MBE has produced lattice-matched, high-quality superlattices, there remains room to improve interface sharpness and compositional uniformity, thereby enhancing device performance. Third, the fabrication process can be further optimized, particularly in mesa definition and contact metallization, to reduce device-to-device variability. In addition, surface passivation can further suppress surface leakage, thereby reducing dark current. Finally, applying an optimized anti-reflection coating on the device window can improve the coupling efficiency of incident light, further enhancing the device's photoresponse and quantum efficiency. These improvements will lay the foundation for higher-performance and more competitive e-SWIR light detectors.

8.Reference

[1] F. Cao, L. Liu, and L. Li, “Short-wave infrared photodetector,” *Materials Today*, vol. 62, pp. 327–349, 2023.

[2] W. Shen, J. Du, L. Sun, C. Wang, Y. Zhu, K. Xu, B. Chen, and Z. He, “Low-latency and high-speed hollow-core fiber optical interconnection at 2-micron waveband,” *J. Lightwave Technol.*, vol. 38, no. 15, pp. 3874–3882, 2020.

[3] R. Sur, K. Sun, J. B. Jeffries, R. K. Hanson, R. J. Pummill, T. Waind, and K. J. Whitty, “TDLAS-based sensors for in situ measurement of syngas composition in a pressurized, oxygen-blown, entrained flow coal gasifier,” *Appl. Phys. B*, vol. 116, pp. 33–42, 2014.

[4] M. Bashkatov, E. Genina, and V. Tuchin, “Review of short-wave infrared spectroscopy and imaging methods for biological tissue characterization,” *Journal of Biomedical Optics*, vol. 20, no. 3, pp. 030901, 2015.

[5] Q.-S. Wan, T. Wang, and K.-H. Zhang, “Biomedical optical spectroscopy for the early diagnosis of gastrointestinal neoplasms,” *Technology in Cancer Research & Treatment*, vol. 16, no. 6, pp. 791–798, Dec. 2017.

[6] M. Sharma, N. Sharma, and S. R. Kim, “Optical biosensors for detection of cancer biomarkers: Current and future perspectives,” *Biosensors*, vol. 14, no. 2, pp. 142, Feb. 2024.

[7] J. Rutkowski, J. Piotrowski, and A. Rogalski, “Growth and properties of MOCVD HgCdTe epilayers on GaAs substrates,” *Opto-Electron. Rev.*, vol. 13, no. 3, pp. 239–251, 2005.

[8] E. H. Steenbergen, C. P. Morath, D. Maestas, G. D. Jenkins, and J. V. Logan, “Comparing II-VI and III-V infrared detectors for space applications,” in *Proc. SPIE Infrared Technology and Applications XLV*, vol. 11002, pp. 299–307, May 2019.

[9] J. D. Phillips, K. Moazzami, J. Kim, D. D. Edwall, D. L. Lee, and J. M. Arias, “Uniformity of optical absorption in HgCdTe epilayer measured by infrared spectromicroscopy,” Appl. Phys. Lett., vol. 83, pp. 3701–3703, Nov. 2003.

[10] Y. Arslan, F. Oguz, and C. Besikci, “Extended wavelength SWIR InGaAs focal plane array: Characteristics and limitations,” *Infrared Phys. Technol.*, vol. 70, pp. 134–137, 2015.

[11] I. Shafir, D. C. Elias, D. Memram, N. Sicron, and M. Katz, “T2SL/InP/T2SL pBp extended SWIR barriode with InGaAs/GaAsSb absorption material lattice matched to InP,” *Infrared Phys. Technol.*, vol. 125, p. 104217, 2022.

[12] A. Yamamoto, Y. Kawamura, H. Naito, and N. Inoue, “Optical properties of GaAsSb and InGaAs/GaAs Sb type II single hetero-structures lattice-matched to InP substrates grown by molecular beam epitaxy,” J. Cryst. Growth, vol. 201, pp. 872–876, May 1999.

[13] S. Jung *et al.*, “Watt-level continuous-wave antimonide laser diodes with high carrier-confined active region above 2.5 µm,” *Discover Nano*, vol. 19, no. 1, pp. 1–11, 2024.

[14] S. Guo *et al.*, “Room-temperature extended short-wave infrared avalanche photodiode with a 2.6 µm cutoff wavelength,” *Micromachines*, vol. 15, no. 8, p. 941, 2024.

[15] R. T. Huang and D. Renner, “Improvement in dark current characteristics and long-term stability of mesa InGaAs/InP pin photodiodes with two-step SiN/sub x/surface passivation,” *IEEE Photon. Technol. Lett.*, vol. 3, no. 10, pp. 934–936, 1991.

[16] P. Cao, T. Wang, H. Peng, Q. Zhuang, and W. Zheng, “Growth and dark current analysis of GaSb- and InP-based metamorphic In0.8Ga0.2As photodetectors,” *Materials*, vol. 16, no. 13, p. 4538, 2023.

[17] Y. Zhang, Y. Gu, Z. Tian, et al., “Wavelength extended 2.4 µm heterojunction InGaAs photodiodes with InAlAs cap and linearly graded buffer layers suitable for both front and back illuminations,” *Infrared Phys. Technol.*, vol. 51, no. 4, pp. 316–321, 2008.

[18] R. W. Hoogeveen and A. P. Goede, “Extended wavelength InGaAs infrared (1.0–2.4 µm) detector arrays on SCIAMACHY for space-based spectrometry of the Earth atmosphere,” *Infrared Phys. Technol.*, vol. 42, no. 1, pp. 1–16, 2001.

[19] X. Li, J. Xu, T. Wei, W. Yang, S. Jin, Y. Wu, and S. Lu, “Enhanced properties of extended wavelength InGaAs on compositionally undulating step-graded InAsP buffers grown by molecular beam epitaxy,” *Crystals*, vol. 11, no. 12, p. 1590, 2021.

[20] H. Hao, G. Wang, X. Han, D. Jiang, Y. Sun, C. Guo, et al., “Extended-wavelength InGaAsSb infrared unipolar barrier detectors,” AIP Adv., vol. 8, no. 9, 2018.

[21] I. Shafir, N. Snapi, D. Cohen-Elias, A. Glozman, O. Klin, E. Weiss, et al., “High responsivity InGaAsSb p–n photodetector for extended SWIR detection,” *Appl. Phys. Lett.*, vol. 118, no. 6, 2021.

[22] K. Mamic, *Properties of the InGaAsSb Alloy and InGaAsSb-Based Photodiodes*, Ph.D. dissertation, Lancaster Univ., U.K., 2025.

[23] J. F. Klem, J. T. Olesberg, S. D. Hawkins, P. H. Weiner, J. Deitz, C. N. Kadlec, et al., “Extended-short-wavelength infrared AlInAsSb and InPAsSb detectors on InAs,” in *Infrared Technology and Applications XLVII*, vol. 11741, SPIE, 2021, pp. 19–27.

[24] D. Wei, A. A. Dadey, J. A. McArthur, S. R. Bank, and J. C. Campbell, “Enhancing Extended SWIR Al0.3InAsSb PIN Photodetectors with All-Dielectric Amorphous Germanium Photon-Capturing Gratings,” *ACS Photonics*, vol. 11, no. 2, pp. 484–488, 2024.

[25] G. A. Sai-Halasz, R. Tsu, and L. Esaki, “A new semiconductor superlattice,” *Appl. Phys. Lett.*, vol. 30, no. 12, pp. 651–653, 1977.

[26] R. Sidhu, N. Duan, J. C. Campbell, and A. L. Holmes, Jr., “A longwavelength photodiode on InP using lattice-matched GaInAs-GaAsSb type-II quantum wells,” IEEE Photon. Technol. Lett., vol. 17, no. 12, pp. 2715–2717, Dec. 2005.

[27] B. Chen, W. Jiang, J. Yuan, A. L. Holmes, and B. M. Onat, “SWIR/MWIR InP-based pin photodiodes with InGaAs/GaAsSb type-II quantum wells,” *IEEE J. Quantum Electron.*, vol. 47, no. 9, pp. 1244–1250, 2011.

[28] Y. Uliel, D. Cohen-Elias, N. Sicron, I. Grimberg, N. Snapi, Y. Paltiel, and M. Katz, “InGaAs/GaAsSb Type-II superlattice based photodiodes for short wave infrared detection,” *Infrared Phys. Technol.*, vol. 84, pp. 63–71, 2017.

[29] A. Gil, J. Phillips, M. H. Ettenberg, and N. A. Babikir, “Bandgap Engineering and Short-Wavelength Infrared Detection of InGaAs/GaAsSb Superlattices Lattice-Matched to InP,” *J. Electron. Mater.*, vol. 51, no. 9, pp. 4703–4713, 2022.

[30] Y. Liang, W. Zhou, X. Zhang, F. Chang, N. Li, Y. Shan, et al., "InP-based high-performance extended short wavelength pBn infrared photodetector with InGaAs/GaAsSb type-II superlattice absorption layer," *Appl. Phys. Lett.*, vol. 125, no. 14, 2024.

[31] J. F. Klem, O. Blum, S. R. Kurtz, I. J. Fritz, and K. D. Choquette, "GaAsSb/InGaAs type-II quantum wells for long-wavelength lasers on GaAs substrates," *J. Vac. Sci. Technol. B*, vol. 18, no. 3, pp. 1605–1608, 2000.

[32] K. A. Lozovoy, R. M. Douhan, V. V. Dirko, H. Deeb, K. I. Khomyakova, O. I. Kukenov, et al., "Silicon-Based Avalanche Photodiodes: Advancements and Applications in Medical Imaging," *Nanomaterials*, vol. 13, no. 23, p. 3078, 2023.

[33] N. Namekata, S. Sasamori, and S. Inoue, "800 MHz single-photon detection at 1550-nm using an InGaAs/InP avalanche photodiode operated with a sine wave gating," *Opt. Express*, vol. 14, no. 21, pp. 10043–10049, 2006.

[34] J. Chen, J. Chen, X. Li, J. He, L. Yang, J. Wang, et al., "High-performance HgCdTe avalanche photodetector enabled with suppression of band-to-band tunneling effect in mid-wavelength infrared," *npj Quantum Mater.*, vol. 6, no. 1, p. 103, 2021.

[35] H. Jung, S. Lee, X. Jin, Y. Liu, T. J. Ronningen, C. H. Grein, et al., "Low excess noise and high quantum efficiency avalanche photodiodes for beyond 2 μm wavelength detection," *Commun. Mater.*, vol. 5, no. 1, p. 219, 2024.

[36] M. Ali, M. A. Anwar, J. Lv, S. C. Bodepudi, H. Guo, K. Shehzad, et al., "Graphene Field-Effect-Coupled Detection of Avalanche Multiplication in Silicon," *IEEE Trans. Electron Devices*, vol. 70, no. 5, pp. 2370–2377, 2023.

[37] D. Chen, S. D. March, A. H. Jones, Y. Shen, A. A. Dadey, K. Sun, et al., "Photon-trapping-enhanced avalanche photodiodes for mid-infrared applications," *Nat. Photonics*, vol. 17, no. 7, pp. 594–600, 2023.

[38] X. Li, J. Chen, F. Yu, X. Chen, W. Lu, and G. Li, "Achieving a noise limit with a few-layer WSe2 Avalanche Photodetector at Room temperature," *Nano Lett.*, vol. 24, no. 42, pp. 13255–13262, 2024.

[39] S. Adachi, Properties of semiconductor alloys: Group IV, III V and II VI semiconductors. Wiley, 2009.

[40] P. Y. Yu and M. Cardona, ∗Fundamentals of Semiconductors: Physics and Materials

Properties*, 4th ed. Berlin/Heidelberg, Germany: Springer, 2010.

[41] K. Seeger, Semiconductor physics, 9th ed. Springer, 2004.

[42] Y. P. Varshni, "Temperature dependence of the energy gap in semiconductors," *Physica*, vol. 34, pp. 149, 1967.

[43] J. A. Van Vechten and T. K. Bergstresser, "Electronic structures of semiconductor alloys," *Phys. Rev. B*, vol. 1, no. 8, p. 3351, 1970.

[44] C. Klingshirn, Ed., *Landolt-Börnstein - Group III condensed matter: Optical properties of semiconductors*, vol. 34C1. Springer-Verlag, 2001.

[45] S. Adachi, *Properties of Semiconductor Alloys: Group-IV, III-V and II-VI Semiconductors*. Hoboken, NJ, USA: John Wiley & Sons, 2009.

[46] R. Dingle, W. Wiegmann, and C. H. Henry, "Quantum states of confined carriers in very thin $Al_xGa_{1-x}As$–GaAs–$Al_xGa_{1-x}As$ heterostructures," *Physical Review Letters*, vol. 33, no. 14, pp. 827–830, Oct. 1974.

[47] S. M. Sze, Y. Li, and K. K. Ng, Physics of Semiconductor Devices, John Wiley & Sons, 2021.

[48] R. F. Pierret, *Semiconductor Device Fundamentals*. Reading, MA, USA: Addison-Wesley, 1996.

[49] W. Shockley, "The theory of p-n junctions in semiconductors and p-n junction transistors," Bell Syst. Tech. J., vol. 28, no. 3, pp. 435–489, Jul. 1949.

[50] C. Hu, "Carrier injection under forward bias—quasi-equilibrium boundary condition," in *PN and Metal–Semiconductor Junctions*, ch. 4, pp. 104–105.

[51] K. Lehovec, C. A. Accardo, and E. Jamgochian, "Injected light emission of silicon carbide crystals," Phys. Rev., vol. 83, p. 603, 1951.

[52] S. Sze and L. Ming-Kwei, Semiconductor Devices: Physics and Technology, third. John Wiley & Sons Singapore Pte. Limited, 2012.

[53] A. M. Joshi and G. H. Olsen, "Photodetection—Semiconductors," in Handbook of Optics, 3rd ed., McGraw-Hill, ch. 16.

[54] F. A. Lindholm, "Phenomena simulation for heavy doping and surface recombination velocity," in Proc. Flat-Plate Solar Array Project Res. Forum on High-Efficiency Crystalline Silicon Solar Cells, May 1985.

[55] J. K. Katahara and H. W. Hillhouse, "Quasi-Fermi level splitting and sub-bandgap absorptivity from semiconductor photoluminescence," *J. Appl. Phys.*, vol. 116, no. 17, p.

173504, Nov. 2014.

[56] K. Taretto, U. Rau, and S. Siebentritt, “Numerical simulation of carrier collection and recombination in chalcopyrite solar cells,” *J. Appl. Phys.*, vol. 103, p. 094523, May 2008.

[57] H. Spieler, Introduction to Radiation Detectors and Electronics, VI. Position-Sensitive Detectors, 1998.

[58] R. A. Smith, Semiconductors, 2nd ed. Cambridge, U.K.: Cambridge Univ. Press, 1978, ch. 8, sec. 8.3.

[59] P. W. M. Blakers, A. Wang, and E. S. Witt, “High-efficiency silicon solar cells,” IEEE Trans. Electron Devices, vol. 31, no. 5, pp. 637–647, May 1984.

[60] G. Parker, Introductory semiconductor device physics. Prentice Hall International, 1994.

[61] Chapuis G. An elementary treatment on the diffraction of crystalline structures. Crystallography Reviews. 2021 10; 27:146-77.

[62] The Editors of Encyclopaedia Britannica, “X-ray diffraction,” *Encyclopedia Britannica*, 2024. [Online]. Available: https://www.britannica.com/science/X-ray-diffraction

[63] Gilliland GD. Photoluminescence spectroscopy of crystalline semiconductors. Materials Science and Engineering: R: Reports. 1997; 18:99-399.

[64] Lock-in Amplifiers Tutorial. Bentham Instruments; 2017. Available from: https://support.bentham.co.uk/support/solutions/articles/ 13000036065-lock-in-amplifier-tutorial.

[65] I. Malashin, D. Daibagya, V. Tynchenko, V. Nelyub, A. Borodulin, A. Gantimurov, and O. Ovchinnikov, “Modeling Temperature-Dependent Photoluminescence Dynamics of Colloidal CdS Quantum Dots Using Long Short-Term Memory (LSTM) Networks,” *Materials*, vol. 17, no. 20, p. 5056, 2024.

[66] A. S. Vokhmintsev, A. N. Pustovarov, and V. Yu. Ivanov, “Temperature effects in 3.9 eV photoluminescence of $Li_2B_4O_7$ single crystals,” *Journal of Luminescence*, vol. 233, p. 117884, Jan. 2021.

[67] Pfeiffer Vacuum, *HiCube Eco Turbo Pumping Stations – Technical Data Sheet*, 2020.

[68] Oxford Instruments, LLT Transfer Siphon Manual, Sep. 2017. Available: https://andor.oxinst.com/downloads/uploads/llt-siphon-user-manual.pdf

[69] Oxford Instruments, OptistatCFV Operation Manual, Sep. 2017. Available: https://andor.oxinst.com/downloads/uploads/optistat-cf-v-user-guide.pdf

[70] Oxford Instruments, Mercury iTC Product Overview. Available: https://nanoscience.oxinst.com/accessories/mercuryitc

[71] Oxford Instruments, *Mercury iTC Product Overview*. [Online]. Available: https://nanoscience.oxinst.com/accessories/mercuryitc

[72] E. R. Menzel, "A time-resolved apparatus involving a mechanical light chopper rotating at 50 Hz," The Scientist, 2004. https://onlinelibrary.wiley.com/doi/pdf/10.1100/tsw.2004.126

[73] HORIBA Scientific, *iHR Series Mid-Focal Length Imaging Spectrometers (iHR320) Datasheet*.[Online].Available:https://www.horiba.com/usa/scientific/products/detail/action/show/Product/ihr-series-1590/

[74] SR830 Lock-in Amplifier Instruction Manual, Stanford Research Systems. Available upon request from manufacturer.

[75] Horiba Scientific, *Symphony II Detection System – Operation Manual*, May 2025. https://www.horiba.com/fileadmin/uploads/Scientific/Documents/OSD/Total-Symphony-II-Manual.pdf

[76] P. C. Kumar, S. Senapati, M. Pradhan, G. K. Pradhan, and R. Naik, "Laser power and high-temperature dependent Raman studies of layered bismuth and copper-based oxytellurides for optoelectronic applications," *Phys. Chem. Chem. Phys.*, vol. 26, pp. 12231–12245, 2024.

[77] G. Lu, "Temperature dependence of Raman scattering of ZnSe nanoparticles," *J. Crystal Growth*, vol. 274, pp. 530–535, 2005.

[78] S. O. Kasap, *Principles of Electronic Materials and Devices*. New York, NY, USA: McGraw-Hill, 2006.

[79] A. Rogalski and K. Chrzanowski, "Infrared devices and techniques," *Opto-Electronics Review*, vol. 10, no. 2, pp. 111–136, 2002.

[80] J. W. Matthews and A. E. Blakeslee, "Defects in epitaxial multilayers: I. Misfit dislocations," J. Cryst. Growth, vol. 27, pp. 118–125, 1974.

[81] B.R. Wu, J.Y.T. Huang, J. Meyer, et al., "Growth optimization of GaAsSb lattice matched to InP by molecular beam epitaxy," *J. Vac. Sci. Technol. B*, vol. 23, no. 4, pp. 1641–1645, Jul. 2005.

[82] D.P. Xu, J.Y.T. Huang, J. Meyer, et al., "Characteristics of dilute-nitride GaAsSbN/InP strained multiple quantum wells," *J. Appl. Phys.*, vol. 101, no. 5, p. 053104, Mar. 2007.

[83] Y. Lyu, et al., "Digitally grown AlInAsSb for high gain separate absorption, grading, charge,

and multiplication avalanche photodiodes," *J. Cryst. Growth*, vol. 482, pp. 70–75, 2018.

[84] D. M. Cornet and R. R. LaPierre, "High resolution x-ray diffraction analysis of InGaAs/InP superlattices," *J. Appl. Phys.*, vol. 100, no. 12, p. 123510, 2006.

[85] A. R. Clawson, "Guide to references on III–V semiconductor chemical etching," *Mater. Sci. Eng. R Rep.*, vol. 31, no. 1, pp. 1–438, 2001.

[86] H. Inada et al., "Low dark current SWIR photodiode with InGaAs/GaAsSb Type II quantum wells grown on InP substrate," in *Proc. IEEE Int. Conf. Indium Phosphide Rel. Mater.*, Newport Beach, CA, USA, May 2009, pp. 149–152.

[87] S. H. Kodati et al., "AlInAsSb avalanche photodiodes on InP substrates," *Appl. Phys. Lett.*, vol. 118, no. 9, p. 091101, Mar. 2021.

[88] Y. Ji, "InGaAs/GaAsSb type-II superlattice (lattice matched to InP substrates)," Ph.D. thesis, Univ. of Sheffield, UK, 2022.

[89] R. Sidhu et al., "A long-wavelength photodiode on InP using lattice-matched GaInAs-GaAsSb type-II quantum wells," *IEEE Photon. Technol. Lett.*, vol. 17, no. 12, pp. 2715–2717, Dec. 2005.

[90] B. Chen et al., "SWIR/MWIR InP-based p-i-n photodiodes with InGaAs/GaAsSb Type-II quantum wells," *IEEE J. Quantum Electron.*, vol. 47, no. 9, pp. 1244–1250, Sep. 2011.

[91] A. E. Zhukov et al., "Influence of mismatch of the lattice parameters on the structural, optical, and transport properties of InGaAs layers grown by molecular beam epitaxy on InP (100) substrates," *Semiconductors*, vol. 31, pp. 15–18, Jan. 1997.

[92] B. Smiri et al., "Optical and structural properties of In-rich $In_xGa_{1-x}As$ epitaxial layers on (100) InP for SWIR detectors," *Semicond. Sci. Technol.*, 2020.

[93] J. Stangl, V. Holy, and G. Bauer, "Structural properties of self-organized semiconductor nanostructures," *Rev. Mod. Phys.*, vol. 76, no. 3, pp. 725–783, 2004.

[94] H. M. Jia, L. Shen, X. Li, Y. Kang, X. Fang, D. Fang, F. Lin, J. Tang, D. K. Wang, X. Ma, Z. Wei, "Investigation of localized state emissions in quaternary InGaAsSb/AlGaAsSb multiple quantum wells grown by molecular beam epitaxy," *Optical Materials Express*, vol. 12, no. 12, p. 3384, Dec. 2020.

[95] Y. S. Chiu, M. H. Ya, W. S. Su, and Y. F. Chen, "Properties of photoluminescence in type-II GaAsSb/GaAs multiple quantum wells," *J. Appl. Phys.*, vol. 92, no. 10, pp. 5810–5813, Nov. 2002.

[96] M. Jo, M. Sato, S. Miyamura, H. Sasakura, H. Kumano, and I. Suemune, "Origin of the blueshift of photoluminescence in a type-II heterostructure," *Nanoscale Res. Lett.*, vol. 7, art. no. 654, Nov. 2012.

[97] A. S. Vokhmintsev and I. A. Weinstein, "Temperature effects in 3.9 eV photoluminescence of hexagonal boron nitride under band-to-band and subband excitation within 7–1100 K range," *Journal of Luminescence*, vol. 230, p. 117623, 2021.

[98] J. F. Klem, O. Blum, S. R. Kurtz, I. J. Fritz, and K. D. Choquette, "GaAsSb/InGaAs type-II quantum wells for long-wavelength lasers on GaAs substrates," *J. Vac. Sci. Technol. B*, vol. 18, no. 3, pp. 1605–1608, 2000.

[99] S. Martini, A. A. Quivy, A. Tabata, and J. R. Leite, "Influence of the temperature and excitation power on the optical properties of InGaAs/GaAs quantum wells grown on vicinal GaAs (001) surfaces," *J. Appl. Phys.*, vol. 90, no. 5, pp. 2280–2289, 2001.

[100] J. Y. T. Huang, L. J. Mawst, T. F. Kuech, X. Song, S. E. Babcock, C. S. Kim, I. Vurgaftman, J. R. Meyer, and A. L. Holmes, "Design and characterization of strained InGaAs/GaAsSb type-II 'W' quantum wells on InP substrates for mid-IR emission," *Journal of Physics D: Applied Physics*, vol. 42, no. 2, p. 025108, 2009.

[101] "The structural and optical properties of GaSb/InGaAs type-II quantum dots grown on InP (100) substrate," Discover Nano, 2012.

[102] Q. Li, S. J. Xu, M. H. Xie, and S. Y. Tong, "Interpretation of the 'S-shaped' temperature dependence of luminescent peaks from semiconductors," arXiv preprint arXiv: Cond-mat/0502074, 2005.

[103] M. Dixit, S. Porwal, S. D. Singh, T. K. Sharma, S. Ghosh, and S. M. Oak, "A versatile phenomenological model for the S-shaped temperature dependence of photoluminescence energy for an accurate determination of the exciton localization energy in bulk and quantum well structures," Journal of Physics D: Applied Physics, vol. 47, no. 6, p. 065103, 2014.

[104] W. Xiong, Y. Chen, H. Xu, H. He, and J. Zhang, "Temperature-dependent photoluminescence spectral characteristics of semiconductor nanostructures," Biosensors and Bioelectronics, vol. 94, pp. 686–692, 2017.

[105] Y. Chen, Z. Gong, W. Liu, J. Zhang, and Z. Wu, "Photoluminescence study of the interface fluctuation effect for InGaAs/InAlAs/InP single quantum well with different thickness,"

Scientific Reports, vol. 7, no. 1, p. 4451, 2017.

9.Appendix

1. The procedure of using liquid helium

BEFORE EXPERIMENT

1. Before using Helium: tell Harald 1 week before,

If you don't: might maybe have helium maybe not

2. Close dewar valve and valve at the wall and detach the dewar from the return line.
3. Weigh dewar
4. Write down on list: name, number dewar, weigh before use, cost code
5. Bring dewar to your lab
6. In your lab: attach the dewar to the lab return line
7. Open the dewar valve and the lab return line

AFTER EXPERIMENT

1. Close dewar valve and the lab return line
2. Detach dewar from lab return line
3. Move dewar back to helium room(A512)
4. Weigh dewar
5. Write down on list: weigh after use, amount of Helium (L)： （weigh before-weigh after）×8, date
6. Attach dewar to return line in A512
7. Open valve on dewar and valve at the wall of return line in A512

2.Gas cylinder safety

Cylinder storage

Fixed to walls or work benches or support structures with chains or straps

Regulator change

1.Before the regulator change

A. Be clear which gas you use and at which pressure
B. Check the specification of the regulator
C. Check the replacement date of the regulator
D. Check the outlet on the cylinder and the connector of the regulator for apparent damage

2.Regulator change: detach

3.Regulator change: attach (Don’t forget to spray the connection you just made with a leak detector spray)

3. Transfer liquid N2

The filling procedure:

1. open vent valve
2. close auto pressure build
3. connect the fill hose
4. open the fill valve
5. insert the auto cut-off probe
6. start the filling
7. manual filling stop
8. automatic filling stop
9. detaching the dewar
10. Record of usage

4.The Procedure of X-Ray Scanning

1. Putting sample on the table, connect with power supply.
2. Changing voltage and current to forty and click “set”
3. Changing Psi-H to 0 degrees, Primar y Rotary Absc to 76.1, scan type to” z”, then, click “start”. Find the middle of mill spindle and double click.
4. Change scan type to “Rocking curve” and change omega -2 to 2 and change total time by changing the number in the middle. Click the “start”, click ‘commander ‘in the taskbar above. And click ’reference’, and click ’apply’. Repeat the above two steps for at least three times.
5. Changing the angle of ‘Omega H’ and ‘Theta2-H’ to the corresponding materials which is written in the wall. The scan type is Rocking Curve, and change the number of Omega in the scan setup, change the number to two digits before and after the first data, and double click the peak.
6. Changing the time again, such as: changing 0.01 to 0.001, makes the time reasonable, and change ‘Primar RotarAbsc’ to ‘Auto’, then click ‘start’.
7. Changing scan type to Twotheta, change the Omega to two digits before and after the data which makes the time reasonable, click the peak. Repeat the above two steps until the number change becomes minimal.
8. Change the scan type to ‘Omega 2Theta’, from 30 to 33 (if OmegaH is 31), the time can be 600s, and change the ordinate from Y to logy.
9. Save to a file, select the third format, and write the sample name. Finally, change correspondent numbers to 0 0 90 0 76.1, and click ‘3.45’, and finally change the voltage and current to 20, 5, click ’set’.
10. Open model., write down the relevant models, the first one is InGaAs, the second one is Inp, and all the dimensions should be written, with the content of 0.52. Open graph and press to start building Action property transform, and keep pressing to change the value of X, such as x-0.001, to match the highest peak.

No.	Structure	T	V	λ_p	FWHM	Intensity
A1597	InGaAs on InP	8K	60mW	1559.131	26.732	637.058
A1597	InGaAs on InP	8K	80mW	1557.348	29.367	867.847
A1597	InGaAs on InP	8K	100mW	1559.854	36.664	896.458
A1597	InGaAs on InP	8K	120mW	1558.868	32.464	1169.210
A1597	InGaAs on InP	8K	140mW	1559.297	32.462	1253.140
A1636	InGaAs on InP	8K	60mW	1545.558	30.787	421.526
A1636	InGaAs on InP	8K	80mW	1544.510	39.917	469.210
A1636	InGaAs on InP	8K	100mW	1543.637	35.678	610.355
A1636	InGaAs on InP	8K	120mW	1544.150	36.300	703.815
A1636	InGaAs on InP	8K	140mW	1542.672	34.000	875.477

No.	Structure	T	V	λ_p	FWHM	Intensity
A1805	GaAsSb on InP	8K	40mW	1757.316	83.68138	83.68138
A1805	GaAsSb on InP	8K	60mW	1747.564	96.8447	1359.95
A1805	GaAsSb on InP	8K	80mW	1740	45.42628	1651.77
A1805	GaAsSb on InP	8K	100mW	1758.095	83.09276	2033.25
A1805	GaAsSb on InP	8K	120mW	1757.456	73.95542	2477.66
A1805	GaAsSb on InP	8K	140mW	1750.621	87.52489	3122.34

No.	Structure	T	V	λ_p	FWHM	Intensity
A1840	AlInAsSb on GaSb	8K	80mW	2390.389	92.176	684.742
A1840	AlInAsSb on GaSb	8K	100mW	2381.125	81.928	717.167
A1840	AlInAsSb on GaSb	8K	120mW	2403.909	146.221	597.004
A1840	AlInAsSb on GaSb	8K	140mW	2380.671	99.093	770.573
A1840	AlInAsSb on GaSb	10K	140mW	2379.149	124.173	919.346
A1840	AlInAsSb on GaSb	20K	140mW	2401.850	227.217	469.210

No.	Structure	T	V	λ_p	FWHM	Intensity
A1869	AlInAsSb on GaSb	8K	60mW	2399.537	44.674	513.081
A1869	AlInAsSb on GaSb	8K	80mW	2382.334	140.312	619.892
A1869	AlInAsSb on GaSb	8K	100mW	2386.660	127.348	679.020
A1869	AlInAsSb on GaSb	8K	120mW	2383.061	110.395	589.374
A1869	AlInAsSb on GaSb	8K	140mW	2382.491	96.790	946.049
A1869	AlInAsSb on GaSb	10K	140mW	2383.114	112.129	1094.830
A1869	AlInAsSb on GaSb	20K	140mW	2387.167	107.956	717.167
A1869	AlInAsSb on GaSb	30K	140mW	2391.506	106.989	549.320

No.	Structure	T	V	λ_p	FWHM	Intensity
A1788	InGaAs/GaAsSb SL on InP	8K	20mW	2368.498	164.088	610.355
A1788	InGaAs/GaAsSb SL on InP	8K	40mW	2297.026	176.581	1312.264
A1788	InGaAs/GaAsSb SL on InP	8K	60mW	2257.412	195.146	1922.612
A1788	InGaAs/GaAsSb SL on InP	8K	80mW	2220.172	229.819	2624.531
A1788	InGaAs/GaAsSb SL on InP	8K	100mW	2193.003	256.989	3417.981
A1788	InGaAs/GaAsSb SL on InP	8K	120mW	2174.926	237.273	4333.532
A1788	InGaAs/GaAsSb SL on InP	8K	140mW	2157.691	251.592	5096.471

No.	Structure	T	V	λ_p	FWHM	Intensity
A1792	InGaAs/GaAsSb SL on InP	8K	20mW	2342.721	150.1962	392.916
A1792	InGaAs/GaAsSb SL on InP	8K	40mW	2272.661	177.5952	740.055
A1792	InGaAs/GaAsSb SL on InP	8K	60mW	2223.786	227.9147	1186.38
A1792	InGaAs/GaAsSb SL on InP	8K	80mW	2183.178	250.5623	1800.54
A1792	InGaAs/GaAsSb SL on InP	8K	100mW	2157.408	299.7296	3417.98
A1792	InGaAs/GaAsSb SL on InP	8K	120mW	2146.191	301.7229	4241.97

A1792	InGaAs/GaAsSb SL on InP	8K	140mW	2137.268	269.8936	5188.02

T2SL	type II InGaAs/GaAsSb superlattice
XRD	X-ray diffraction
PL	Photoluminescence
SWIR	shortwave infrared band
e-SWIR	extended shortwave infrared band
CBM	conduction band minimum
As	arsenic
Al	aluminium
IV	Current-Voltage
LIA	lock-in amplifier
DUT	device under test
ICP	inductive coupled plasma
Eg	bandgap energy